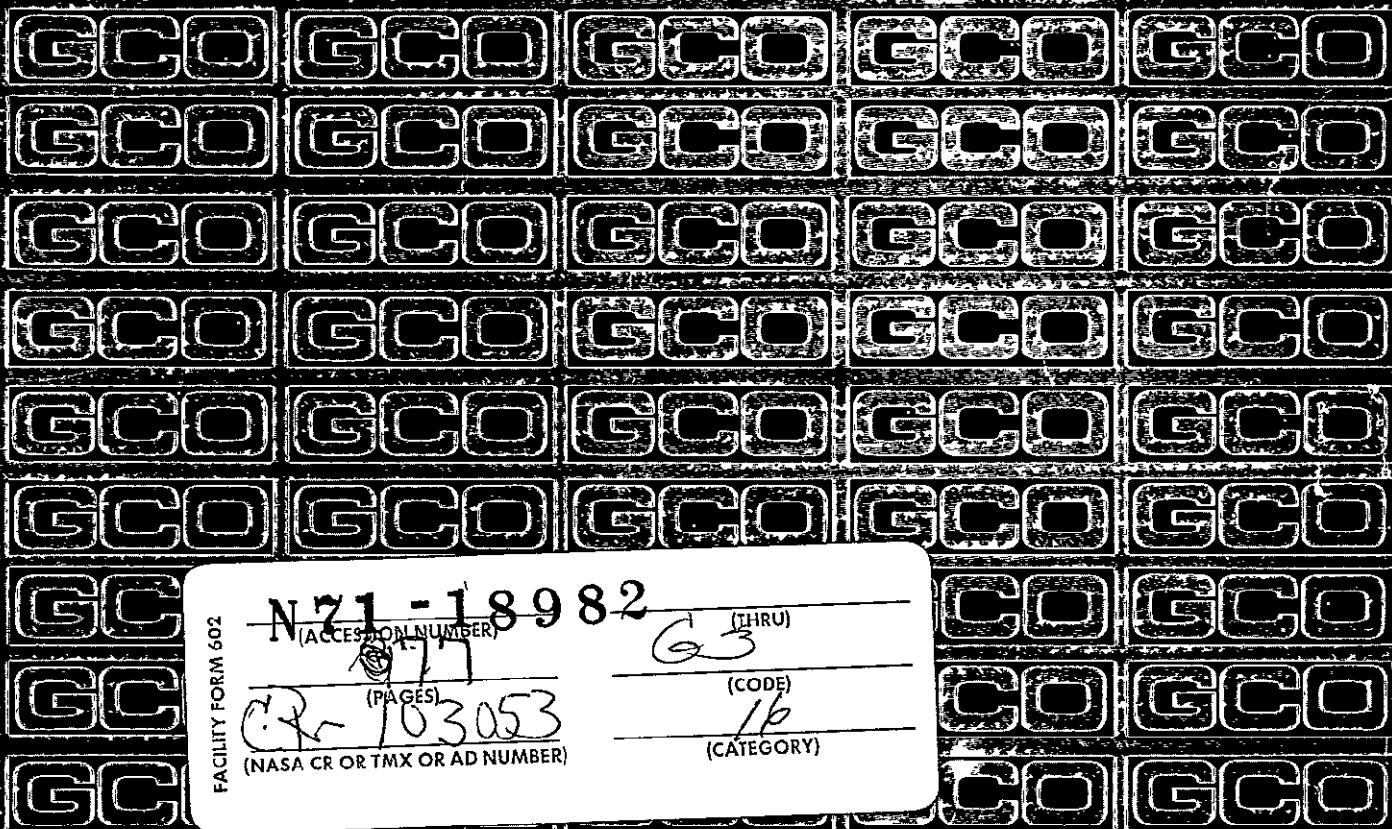




VIBRATION, FLUTTER, AND TRANSIENT  
ANALYSIS USING HOLOGRAPHIC METHODS



Reproduced by  
NATIONAL TECHNICAL  
INFORMATION SERVICE  
Springfield, Va. 22151

GCO-70001  
June 30, 1970

VIBRATION, FLUTTER,  
AND TRANSIENT ANALYSIS  
USING HOLOGRAPHIC METHODS

Contract No. NAS8-21369  
Final Report  
June 1970

Prepared for

National Aeronautics and Space Administration  
George C. Marshall Space Flight Center  
Marshall Space Flight Center, Alabama 35812

GCO, Inc.  
3901 South State Road  
Ann Arbor, Michigan 48104

## ABSTRACT

GCO, Inc. has investigated, under Contract No. NAS8-21369, the application of holographic interferometric methods to vibration, flutter, and transient analysis of thin, metallic panels to be used in space stations. These panels were simulated by various aluminum and steel panels which were studied using time-average holography to determine mode shape of the vibrating panel. Real-time holography was used with special phase-shifting techniques to determine phase of the vibrating panels. Transient-response analysis was done with real-time holography and a high-speed camera.

Time-average holography was shown to be a useful tool in determining vibrational mode patterns of a panel. Mode patterns on vibrating objects were shown to agree with the theory. Amplitude measurement from the holographic data was verified using an optical interferometer to measure amplitude at the center of the vibrating plate. The agreement of these two measurements was very good. The technique was also applied to a thin-walled cylinder provided by NASA.

Two phase-measurement techniques were demonstrated. One approach used a phase-shifted reference beam which allows the operator to control the apparent mode position and thereby determine the phase at that position. The other approach utilized a strobe technique to "freeze" the observed real-time fringes. By varying the relative phase of the strobed light to the panel, the operator can measure relative phases on the vibrating panel.

Transient-response analysis was shown to be feasible with the aid of a high-speed motion-picture camera. An image-converter tube camera was tried, but the light levels were too low to be photographed. Two sets of high-speed movie tests were run--the first on the NASA-provided cylinder. A high-speed movie of the real-time fringe system showed the result of hitting the cylinder with a small steel ball. Analysis of the vibrational modes of cylinders is too difficult for good transient analysis. The test was repeated on a small circular plate and was extended to include studies of the transient response to removal of a steady-state forcing function, a step-function impulse, and shock impulse.

## CONTENTS

ABSTRACT	<u>Page</u> ii
FIGURES	
1.0 INTRODUCTION	1-1
1.1 Objective of Contract	1-1
1.2 Statement of the Problem	1-1
1.3 Summary of Techniques Investigated	1-1
2.0 TIME-AVERAGE HOLOGRAPHIC INTERFEROMETRY	2-1
2.1 Theory	2-1
2.2 Experimental Approach	2-3
2.3 Results	2-7
2.4 Verification of Data by Optical Interferometry	2-19
2.5 Application Limitations	2-26
3.0 PHASE-SHIFTED REFERENCE BEAM	3-1
3.1 Theory	3-1
3.2 Application of Phase-Shifted Reference Beam	3-6
3.3 Experimental Verification of Phase-Shifted Reference-Beam Method	3-10
4.0 SHUTTERED-LASER PHASE MEASUREMENT	4-1
4.1 Theory	4-1
4.2 Pulse-Length Requirement, $\Delta t$ , for Worst Case	4-4
4.3 Pulse-Length Requirement, $\Delta t$ , for Best Case	4-6
4.4 Experimental Verification of Shuttered-Laser Phase Measurement	4-9
5.0 TRANSIENT ANALYSIS RESPONSE	5-1
5.1 Image-Converter Camera	5-1
5.2 High-Speed Camera	5-2
6.0 CONCLUSION AND RECOMMENDATIONS	6-1
6.1 Steady-State Vibrational Analysis	6-1
6.2 Stroboscopic Analysis	6-2
6.3 Shock	6-2
6.4 Recommendations	6-3

## Figures

	<u>Page</u>
2-1 Illumination, Observation and Vibration Geometry	2-2
2-2 Schematic Diagram of Holographic Interferometric System for Time-Average Vibration Analysis	2-5
2-3 Holding Fixture for Rectangular Steel Panel	2-6
2-4 Time-Average Holographic Interferograms of Rectangular Steel Panel Vibrating in Resonant Modes	2-8
2-5 Asymmetrical and Diagonal Modes	2-9
2-6 Time-Average Holographic Fringe Patterns of 12-Inch-Square Aluminum Panel at Various Resonance Frequencies, Showing Vibration Mode	2-11
2-7 Time-Average Holographic Interferograms Showing Circumferential Modes in First, Second, and Third Axial Modes of Vibrating Steel Cylinder (4.125-inch diameter, 4.625-inch height, and 0.020-mil thickness)	2-12, 13
2-8 Time-Average Holographic Interferograms of NASA Cylinder Showing Many Vibrational Modes at Various Resonant Frequencies	2-14, 15, 16 & 17
2-9 Schematic Diagram of Optical Interferometer for Measuring Vibration Amplitude	2-20
2-10 Photos of oscilloscope displays of output of optical interferometer: a) recorded just before hologram reconstructed in Fig. 2-11; b), c), d), and e) recorded before hologram reconstructed in Fig. 2-12	2-21
2-11 Reconstruction of time-average hologram of vibrating square panel at fundamental frequency (205 Hz)	2-22
2-12 Reconstruction of time-average hologram of square panel, vibrating at fundamental frequency (205 Hz) but driven with slightly higher power than during recording of Fig. 2-11	2-23
2-13 Vibration-amplitude displacement, determined by holographic interferometry (from Fig. 2-11 and Table 2-I) <u>versus</u> fringe position of a vibrating square plate	2-24

	<u>Page</u>
2-14 Vibration-amplitude displacement, determined by holographic interferometry (from Fig. 2-12 and Table 2-I) <u>versus</u> fringe position of a vibrating square plate	2-25
3-1 Phasor diagram showing object- and reference-wave phasors yielding resultant phasor with magnitude $k\lambda$	3-4
3-2 Phasor diagram for three object points, showing that the minimum phasor resultant is for point 2	3-5
3-3 Phasor diagram showing effect of reference-wave phase variation at constant magnitude	3-7
3-4 Phasor diagram showing effect of reference-wave phase shift with excessive magnitude	3-8
3-5 Schematic Diagram of Holographic Interferometric System for Panel-Vibration Analysis with Phase-Shifted Reference Beam	3-11
3-6 Geometry of Vibrating Mirror, $M_{pz}$ in Reference Beam	3-12
3-7 Reconstructions of time-average holograms, showing the effects of changing magnitude and phase of reference-beam phase shift	3-13
3-8 Reconstructions of time-average holograms, showing the effects of changing magnitude and phase of reference-beam phase shift	3-14
4-1 Maximum Permissible Vibration-Amplitude versus Light-Pulse Duty Cycle to Accurately Freeze Real-Time Fringes in Strobed-Laser Holography	4-10
4-2 Laser Shuttering System	4-11
4-3 Strobed real-time holographic interferometric fringes of a vibrating aluminum panel. Strobe time, 100 $\mu$ sec; frequency, 1300 Hz.	4-12
4-4 Strobed real-time holographic interferometric fringes of a vibrating aluminum panel. Strobe time, 30 $\mu$ sec; frequency, 1300 Hz.	4-13
4-5 Real-time holographic interferometric phase measurement of a circular plate vibrating in (1, 1) mode at 670 Hz	4-14
4-6 Real-time holographic interferometric phase measurement of the same circular plate vibrating in another (1, 1) mode at 700 Hz	4-15

5-1	Exposure time, seconds, for photographs by image-converter camera of reconstructed image of a vibrating plate	5-2
5-2	Real-time holographic interferometric fringe system of 18-inch diameter cylinder photographed by high-speed camera (5000 frames/sec) after shock impulse (frame 2)	5-6

## 1.0 INTRODUCTION

GCO, under contract to the George C. Marshall Space Flight Center, has investigated the feasibility of using holographic interferometric techniques to perform vibration, flutter, and transient analysis of structural panels for earth-orbit space stations. Demonstration of the feasibility of this approach involved the study of time-average holographic techniques, phase-measurement techniques, and high-speed photography of fringe motion.

### 1.1 Objective of Contract

The objective of this effort was to study, investigate, and devise a technique for utilization of holography to determine vibration characteristics of panels to be utilized in space stations (such as the one-year, earth-orbital space station) by performing vibration, flutter, and transient-phenomena analysis during ground testing.

### 1.2 Statement of the Problem

Investigations were designed to demonstrate the feasibility of using holographic interferometry to measure the vibrational characteristics of aerospace structures. The problem was divided into two major parts:

1. Measurement of steady-state vibrations of panels and structures, and
2. Measurement of transient phenomena.

It was desired to measure vibrational amplitudes and phase relationships over the entire structure under consideration. Limitations of the technique as to maximum size of object, accuracy of measurements, and minimum and maximum amplitude were to be defined. Experimental setups were used to verify the proposed techniques. The culmination of this portion of the contract is this final report, a detailed evaluation of all studies conducted.

### 1.3 Summary of Techniques Investigated

The techniques investigated for solving the problems of this contract involved the use of:

1. A helium-neon CW laser and time-average holographic interferometry,
2. A shuttered, high-powered argon CW laser in combination with real-time holographic interferometry, and
3. High-speed movie photography of real-time holographic interferometric fringe patterns.



The first technique was used to measure steady-state vibrating conditions. The second technique was used primarily to measure phase relationships during steady-state vibration. The third technique was used to study the problem of transient phenomena. The specifications and limitations for these techniques were determined from experimental results and extrapolation of equipment used on the experimental work to state-of-the-art equipment, that is, more powerful lasers, lasers with longer coherence lengths, and better shuttering techniques.

## 2.0 TIME-AVERAGE HOLOGRAPHIC INTERFEROMETRY

### 2.1 Theory

An object in space is vibrating with a frequency,  $\omega$  (Fig. 2.1). A point  $(x, y, z)$  on that object at any instant is moving with a direction vector,  $\vec{m}(x, y, z) \sin(\omega t + \beta)$ . If the illumination vector,  $\vec{k}_1$ , makes an angle,  $\Theta_1$ , with the motion vector, and if the observation vector,  $\vec{k}_2$ , is at an angle,  $\Theta_2$ , with the motion vector then the apparent motion,  $\Delta$ , of the point is given by:

$$\begin{aligned} \Delta &= \vec{m} \cdot [\vec{k}_1 + \vec{k}_2] \sin(\omega t + \beta) \\ &= |m(x, y, z)| [\cos \Theta_1 + \cos \Theta_2] \sin(\omega t + \beta) \end{aligned} \quad (2-1)$$

If the object is illuminated with a plane monochromatic wavefront of frequency,  $\Omega$ , the light scattered by the object may be represented by:

$$E_o = A \exp [\Omega t + \phi_o + k \Delta \sin(\omega t + \beta)] \quad (2-2)$$

This wavefront is combined at a hologram plate with a reference wavefront of the form:

$$E_r = B \exp (\Omega t + \phi_r) \quad (2-3)$$

This combination of wavefronts, with its unique pattern of interference fringes, is recorded on the holographic plate. For exposure time,  $\tau$ , the exposure may be represented by:

$$\langle E \rangle = \int_0^\tau \{A^2 + B^2 + 2AB \cos [\phi_r - \phi_o + k \Delta \sin(\omega t + \beta)]\} dt \quad (2-4)$$

and for  $\tau \gg 2\pi/\omega$ , we obtain:

$$\langle E \rangle = \tau (A^2 + B^2) + 2AB\tau J_0(k\Delta) \cos(\phi_r - \phi_o) \quad (2-5)$$

The first term in expression (2-5) is an average background exposure, and the second term contains the information required to reconstruct an image of the object. If the hologram is processed in such a way that its amplitude transmittance is proportional to the exposure, an image reconstructed by a replica of the reference beam may be represented by:

$$\langle I \rangle = \langle I_o \rangle J_0^2(k\Delta) \quad (2-6)$$

where  $\langle I_o \rangle$  represents the reconstructed image of a stationary object. The reconstructed image is an image of the static object, modulated with the fringe

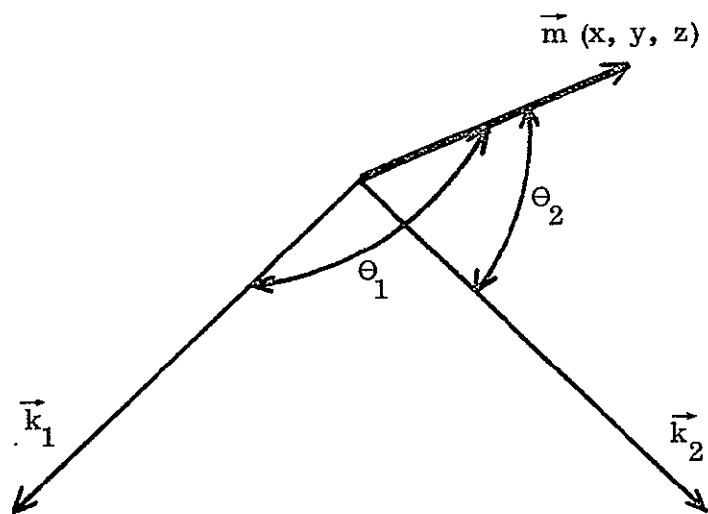


Fig. 2-1. Illumination, Observation and Vibration Geometry

system described by  $J_0^2(k\Delta)$ . Each dark band corresponds to a zero value of  $J_0^2(k\Delta)$  and enables the vibrational amplitude of any point to be determined. Denoting the  $i^{\text{th}}$  root of  $J_0^2(k\Delta)$  as  $\rho_i$ , the vibrational amplitude along a dark fringe may be determined from the equality:

$$\rho_i = (k\Delta) = 2 \pi / \lambda m_i (\cos \Theta_1 + \cos \Theta_2) . \quad (2-7)$$

Values of  $\rho_i$  are tabulated in Table 2-I (column 2) for values of  $i$  (fringe number). The factor  $(\cos \Theta_1 + \cos \Theta_2)$  is called the obliquity factor. For the general case where  $(\cos \Theta_1 + \cos \Theta_2)$  has to be calculated on a point-by-point basis, we have tabulated (column 3):

$$m_i (\cos \Theta_1 + \cos \Theta_2) = \lambda \rho_i / 2\pi . \quad (2-8)$$

For the special case of a plate with  $(m)$  normal to the surface and the optics arranged so that:

$$(\cos \Theta_1 + \cos \Theta_2) \simeq (1 + 1) \simeq 2 , \quad (2-9)$$

we have tabulated in column 4:

$$m_i = \lambda \rho_i / 4\pi . \quad (2-10)$$

## 2.2 Experimental Approach

Vibrational mode patterns of square and rectangular plates and of two cylinders were recorded using time-average holographic interferometry. The holographic setup is shown in Fig. 2-2. The source of coherent light was Coherent Radiation Laboratories Model 52 Argon Ion Laser.

The object was placed in the holographic system such that the illumination and observation angles were small and equal, resulting in an obliquity factor of approximately 2. A large beamsplitter placed in front of the hologram plate permitted the necessary on-axis illumination and on-axis viewing. With this 50-50 beamsplitter, only 25 percent of the object illumination is returned to the plate. To compensate for this loss of light, each object was coated with 3M Scotchlite retro-reflecting material. The light intensity of the wavefront received at the hologram plate from the object was 35 times brighter with retro material, beamsplitter, and on-axis illumination than with diffuse white paint, no beamsplitter and slight off-axis illumination. This coating and illumination geometry were used for all holograms in this study.

The objects were usually driven acoustically with a 12-inch speaker that was excited by a General Radio Oscillator through a Krohn-Hite Amplifier. Some of the observed mode patterns required high driving energies, and the close proximity of lower-order resonances dictated the use of an electromagnetic drive at expected

Table 2-I

Fringe Interpretation

$$J_0(\rho_i) = 0 \quad i = 1, 2, 3 \dots$$

where  $i$  is the number of dark fringes from  $J_0(0)$  (a nodal region)

$$m_i = \frac{\lambda \rho_i}{2\pi (\cos \Theta_1 + \cos \Theta_2)} \quad , \quad \lambda = 0.6328 \mu\text{m} \text{ (632.8 nm)}$$

$$m_i = \frac{0.1007 \rho_i}{(\cos \Theta_1 + \cos \Theta_2)} \mu\text{m}$$

Fringe Number $i$	$\rho_i$	Displacement $m_i (\cos \Theta_1 + \cos \Theta_2)$ ( $\mu\text{m}$ )	Displacement $m_i (\mu\text{m})$ ( $\Theta_1 = \Theta_2 \approx 0$ )
1	2.405	0.242	0.121
2	5.520	0.556	0.278
3	8.634	0.869	0.434
4	11.79	1.187	0.593
5	14.93	1.504	0.751
6	18.07	1.820	0.910
7	21.21	2.136	1.068
8	24.35	2.452	1.226
9	27.49	2.769	1.384
10	30.64	3.086	1.543
11	33.78	3.402	1.701
12	36.92	3.718	1.859
13	40.06	4.035	2.017
14	43.20	4.351	2.175
15	46.34	4.667	2.334
16	49.48	4.983	2.492
17	52.62	5.300	2.650
18	55.77	5.617	2.808
19	58.91	5.933	2.967
20	62.05	6.249	3.125
21	65.19	6.566	3.283
22	68.33	6.882	3.441
23	71.47	7.198	3.599
24	74.61	7.514	3.757
25	77.76	7.832	3.916
26	80.90	8.148	4.074
27	84.04	8.464	4.232
28	87.18	8.780	4.390
29	90.32	9.097	4.548
30	93.46	9.413	4.706

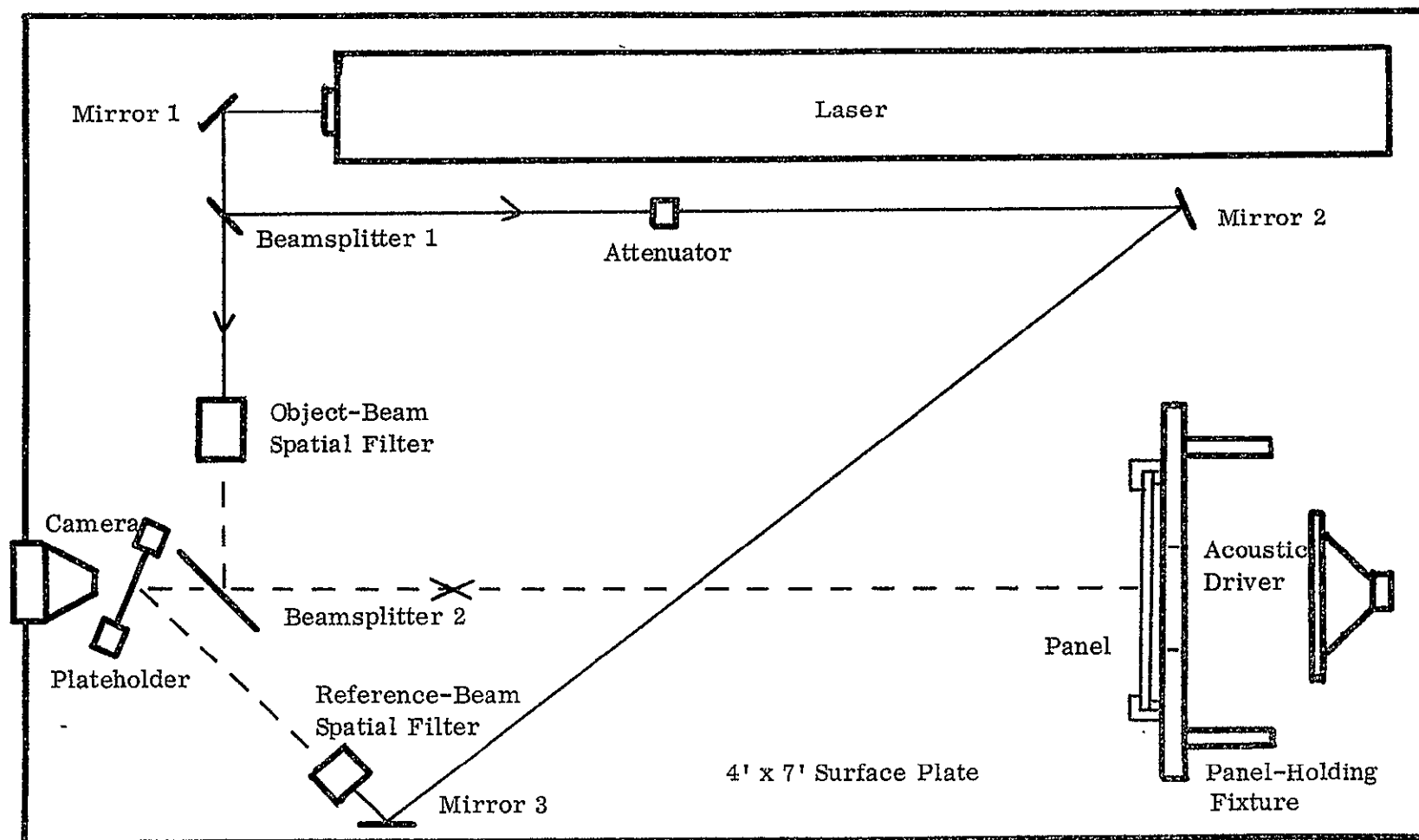


Fig. 2-2. Schematic Diagram of Holographic Interferometric System for Time-Average Vibration Analysis

antinode positions to isolate the desired resonance. Resonant modes were first located by "frequency scanning" during real-time holographic interferometry and recorded by time-average holography at the various resonance frequencies.

A special fixture was built for each object so that the boundary conditions for each object could be well known. Figure 2-3 shows a typical fixture, the one used to support the rectangular steel plate.

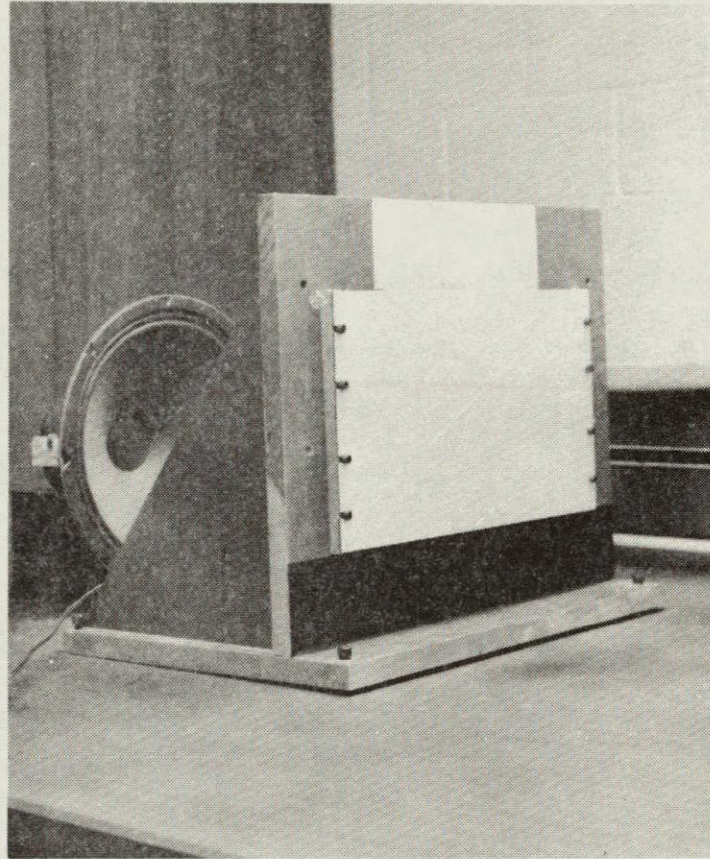


Fig. 2-3. Holding Fixture for Rectangular Steel Panel

The objects analyzed were:

1. Rectangular Panel. A rectangular relay-rack panel, 10 inches by 19 inches by 0.125-inch thick was mounted with the short edges bolted to an aluminum frame. The long edges were unsupported. The presence of fringes between the bolts indicates that the panel was simply supported.

2. Square Panel. A 12-inch-square panel of 0.080-inch aluminum was mounted with all four sides bolted to an aluminum frame. Like the rectangular panel, the square panel was simply supported.

3. Cylinders. Two cylinders were studied by time-average holographic interferometric techniques. The first cylinder was a one-quart paint can, made of 0.020-inch cold-rolled steel, 4.125-inch diameter by 4.625-inch height. The paint can was chosen because of its small size and thin wall. It was placed between two large blocks of iron such that the edges were simply supported.

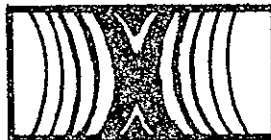
A NASA-supplied cylinder, 18-inch diameter by 27-inch height and made of 0.020-inch aluminum, was studied more extensively. The cylinder was supported vertically and was bolted to a fixture through an angle bracket, which formed the ends of the cylinder. This mounting guaranteed fixed-edge boundary conditions.

## 2.3 Results

### 2.3.1 Rectangular Steel Panel

Typical time-average holographic interferograms of vibrating steel panels are shown in Fig. 2-4 (asterisks indicate electromagnetic excitation). The various orthogonal modes (where the nodal lines are roughly parallel and perpendicular to the edges of the plate) are numbered as follows: the first number corresponds to the number of vertical nodes, and the second number similarly represents the number of horizontal nodes.

In this case the boundary conditions create vertical nodes at both clamped edges, but they are considered as one vertical node. Thus the fundamental resonance mode is a (1,0) mode:



By-and-large, the pictures are self-explanatory. Each dark fringe is a contour of constant vibrational amplitude. Counting dark fringes from a node (denoted by the brightest fringe), one can determine the amplitude of any dark fringe. Table 2-II lists the amplitude in wavelengths for the first 10 fringes.

Interpolation between fringes allows amplitude determination at any point on the surface. To find the amplitude, multiply the amplitude in wavelengths by the wavelength used (or 0.5145 micrometer in this case).



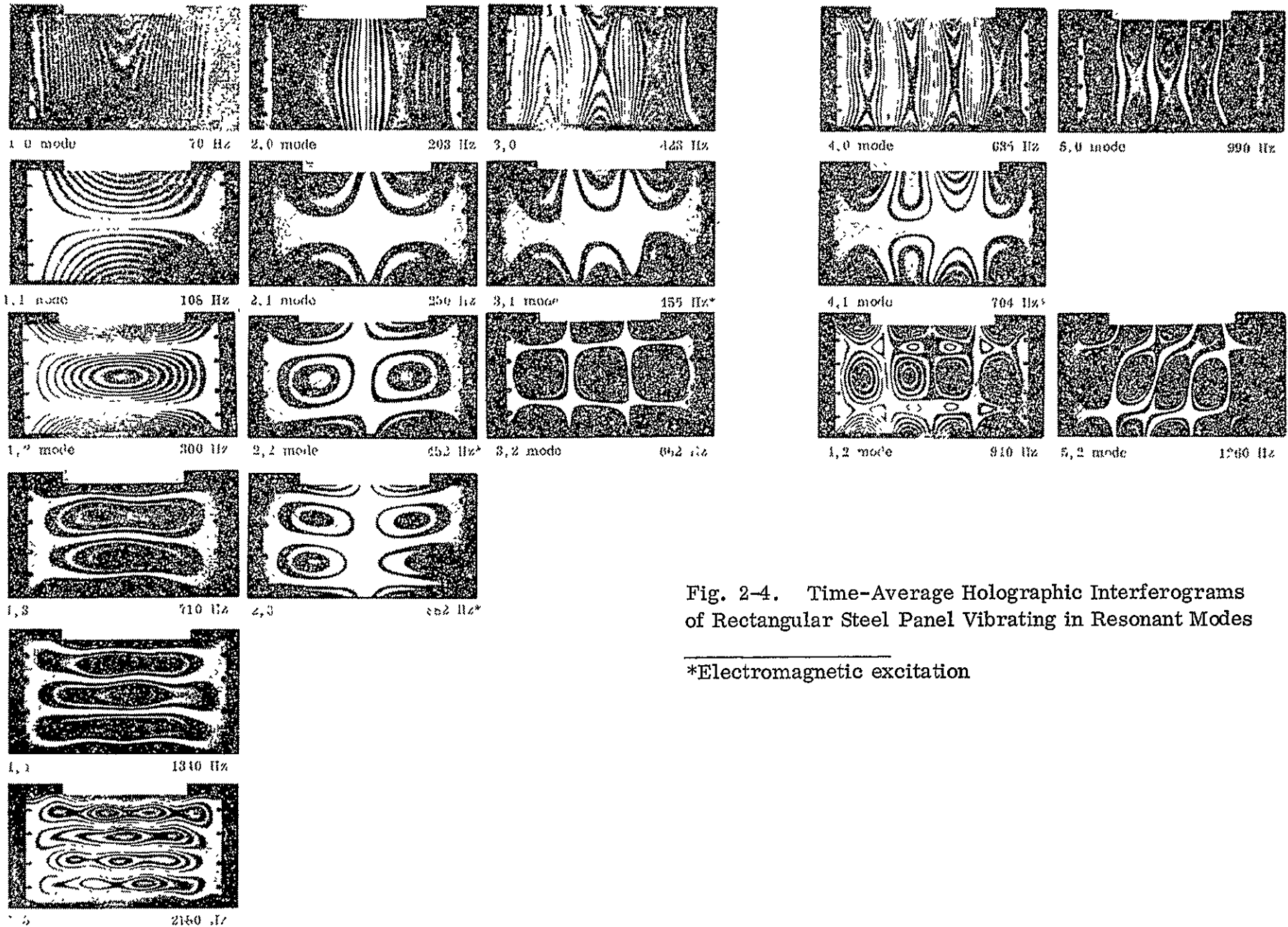


Fig. 2-4. Time-Average Holographic Interferograms of Rectangular Steel Panel Vibrating in Resonant Modes

\*Electromagnetic excitation

Table 2-II

Amplitudes of Dark Fringes on Time-Average Holograms  
of Vibrating Rectangular Steel Panel

<u>i</u>	<u><math>m_i/\lambda</math></u>
1	0.1913
2	0.4392
3	0.6886
4	0.9382
5	1.1881
6	1.4380
7	1.6878
8	1.9377
9	2.1876
10	2.4383

We expected a node at the clamped edges. In the (1,0) and (3,0) modes, however, this mode occurs away from the edges, demonstrating that the holding fixture also has resonances near particular frequencies.

We also noted some asymmetric and diagonal modes, which require a different kind of mode designation. Examples are shown in Fig. 2-5; they may be expected modes (as "a" and "b") or an asymmetric mode (as "c") which does not have at least one axis of symmetry.

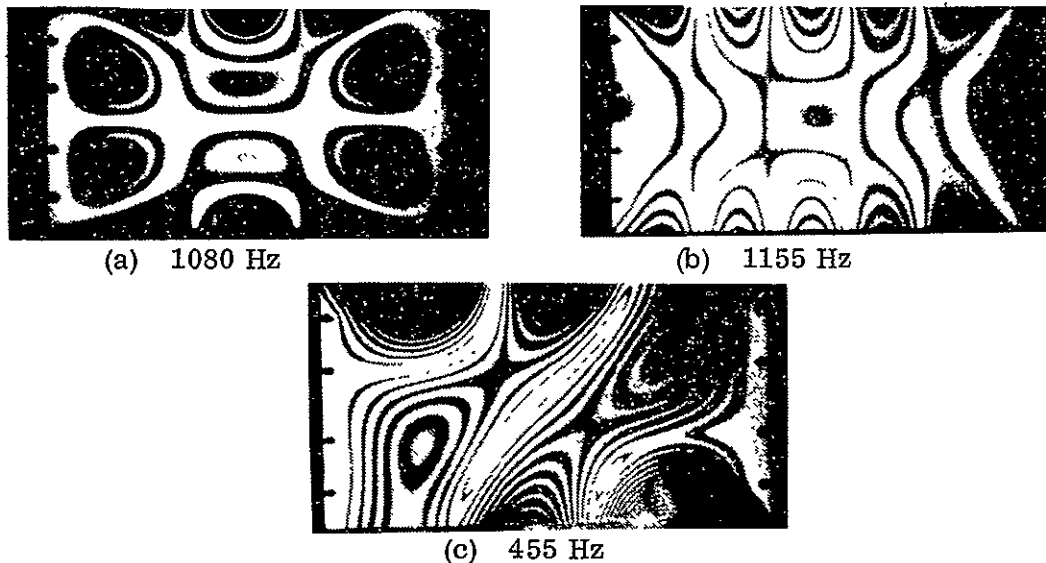


Fig. 2-5. Asymmetrical and Diagonal Modes

### 2.3.2 Square Aluminum Panel

After resonance frequencies were determined by real-time scanning, the time-average holographic interferograms (Fig. 2-6) of a square aluminum panel were made. The mode patterns are not numbered, but the driving frequencies are noted.

### 2.3.3 Small Cylinders

The small cylinder was analyzed to determine feasibility of using the holographic interferometric approach for cylindrical shapes and to assist in determination of the mode characteristics of the larger NASA cylinder. Since only about half of the cylinder was viewed, it is hard to determine exactly the circumferential modes. Two mirrors could be used to provide a 360° view of the cylinder. The cylinder (paint can) was excited electromagnetically. The welded seam at the back near the driver may have affected the mode pattern.

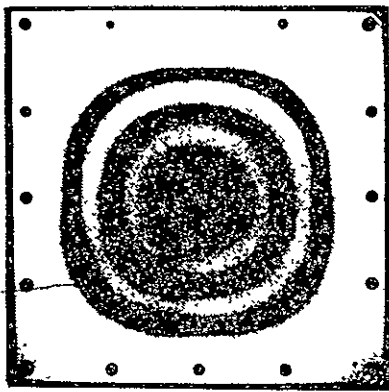
Nine photographs (Fig. 2-7) of reconstructed time-average holographic interferograms of the cylinder vibrating at nine different resonant frequencies show the corresponding circumferential mode, all in the first axial mode. Included also are examples of the same cylinder vibrating in the second and third axial modes and various circumferential modes.

### 2.3.4 Large (NASA) Cylinder

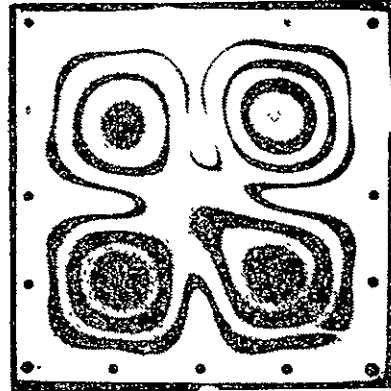
Many time-average holograms of various resonant modes of the 18-inch-diameter NASA cylinder were recorded. Because of the complexity of modes and the duplication of modes at different frequencies, it was difficult to collect and record the data in an orderly manner.

The problem was compounded by the temperature sensitivity of the aluminum cylinder. The cylinder expanded or contracted with only a slight temperature change (less than 1° F) in the lab, causing relatively high-order fringe systems to work with while trying to find various resonances by real-time holographic interferometry. Presence of a thermally induced fringe system makes it difficult to identify various vibrational modes even with strobing, although it is possible to establish that resonance occurs at a particular frequency. A time-average hologram is then recorded at that resonance frequency to identify the mode.

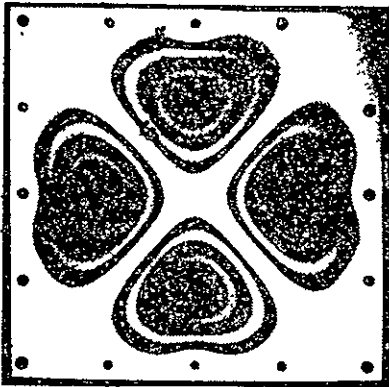
Photographs of these time-average holograms, arranged in mode groups, are presented in Fig. 2-8. Thermal expansion or contraction was insignificant during the relatively short time-average exposures. After holographically recording and photographing several modes we found a pattern that revealed some interesting facts and also helped us locate some missing resonance frequencies. A plotted curve of frequency versus mode number was useful in finding several modes not initially recorded.



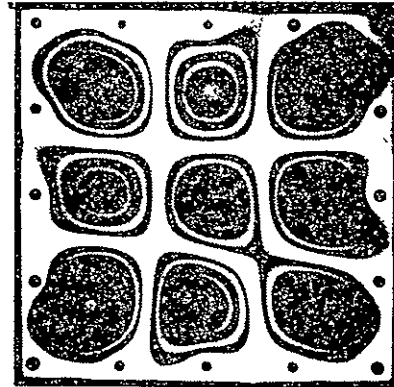
(a) 205 Hz



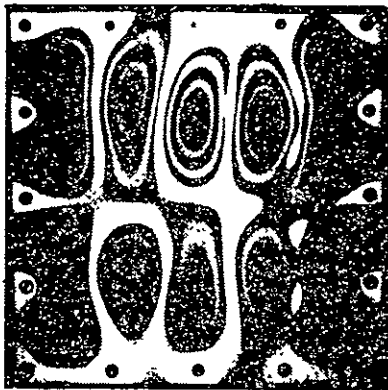
(b) 620 Hz



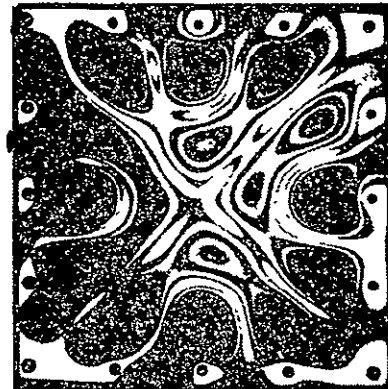
(c) 762 Hz



(d) 1300 Hz



(e) 1972 Hz



(f) 2450 Hz

Fig. 2-6. Time-Average Holographic Fringe Patterns of 12-Inch-Square Aluminum Panel at Various Resonance Frequencies, Showing Vibration Modes

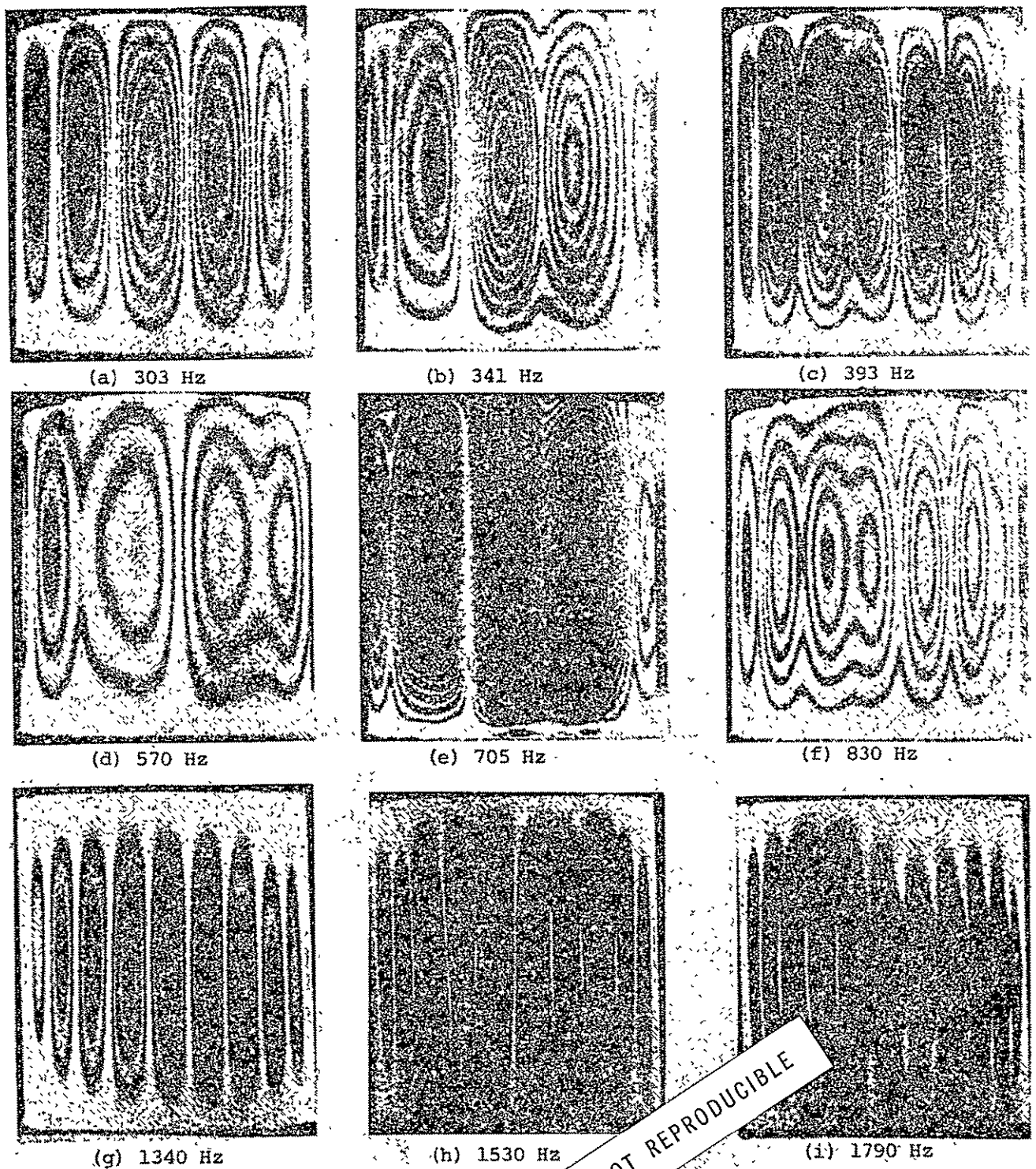
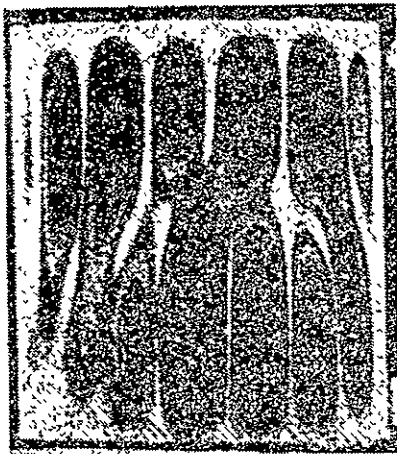
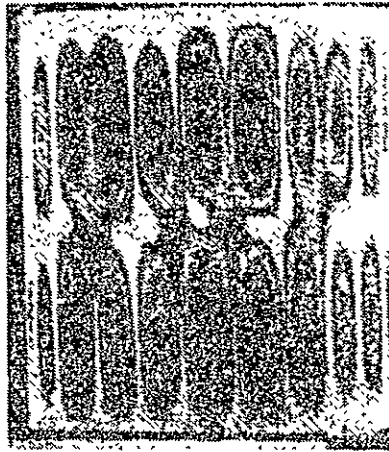


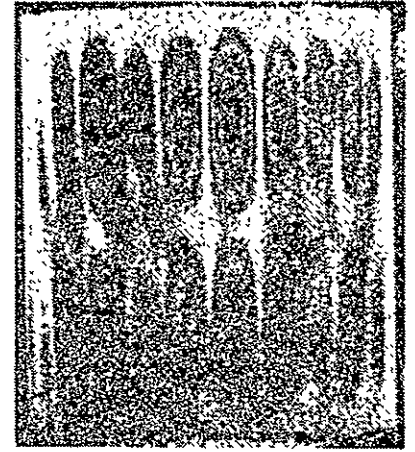
Fig. 2-7. Time-Average Holographic Interferograms Showing Circumferential Modes in First Axial Mode of Vibrating Steel Cylinder (4.125-inch diameter, 4.625-inch height and 0.020-mil thickness)



(a) 1140 Hz

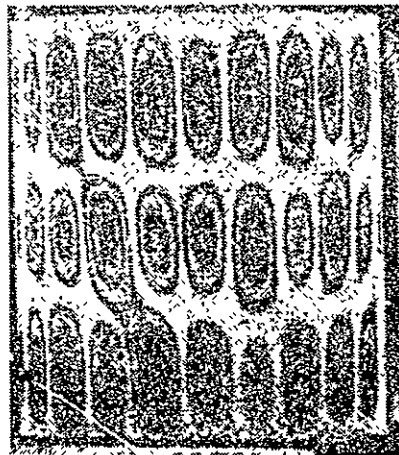


(b) 1480 Hz

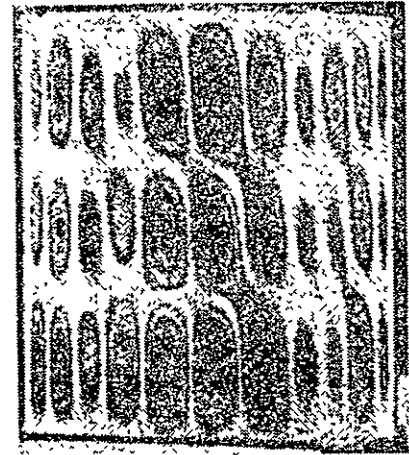


(c) 1650 Hz

(1) Second Axial Mode



(d) 1700 Hz



(e) 1920 Hz

(2) Third Axial Mode

Fig. 2-7. Time-Average Holographic Interferograms of Small Cylinder,  
(cont'd.) Showing Circumferential Modes in Second and Third Axial Modes

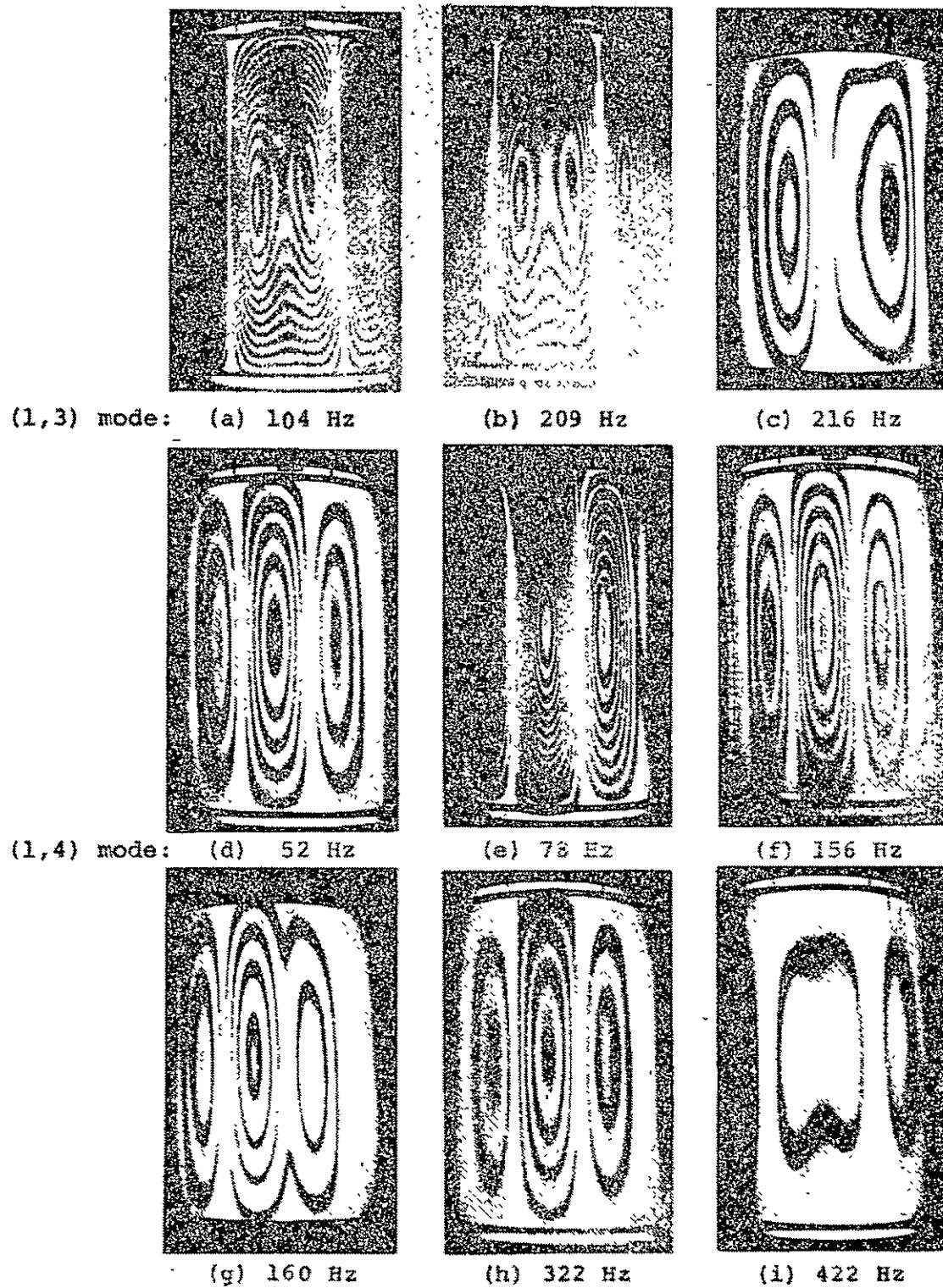


Fig. 2-8. Time-average holograms of NASA cylinder showing (1,3) and (1,4) modes at various frequencies



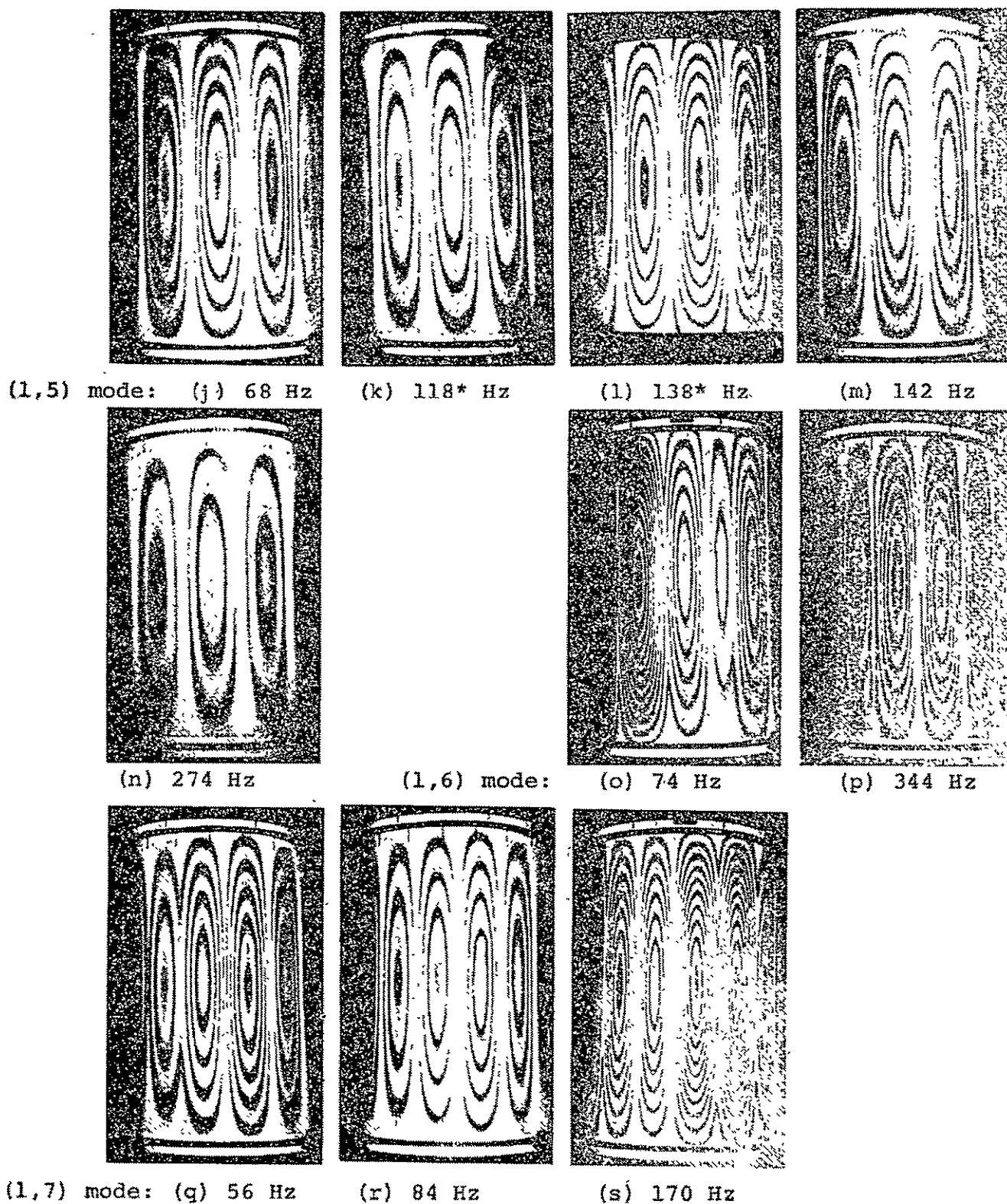


Fig. 2-8. Time-average holograms of NASA cylinder showing (1, 5), (cont'd.) (1, 6), and (1, 7) modes at various frequencies

\*Excited electromagnetically



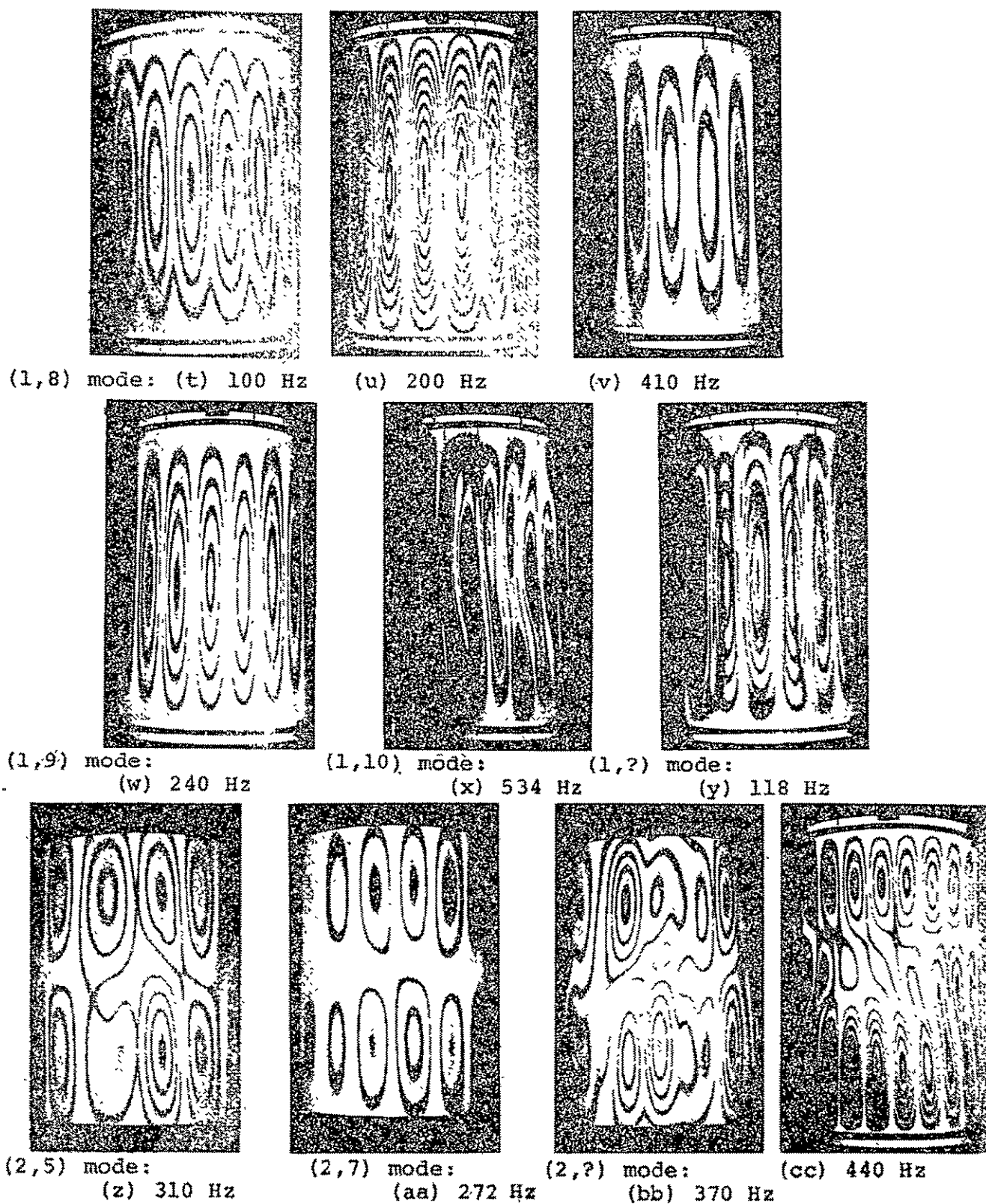
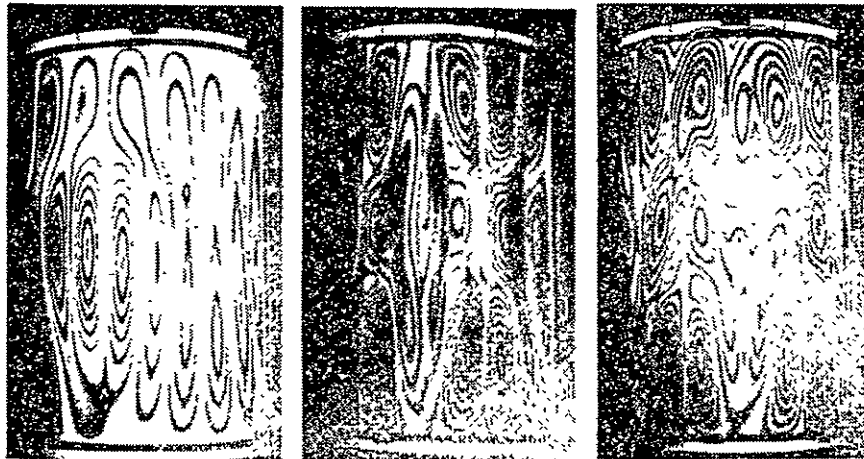
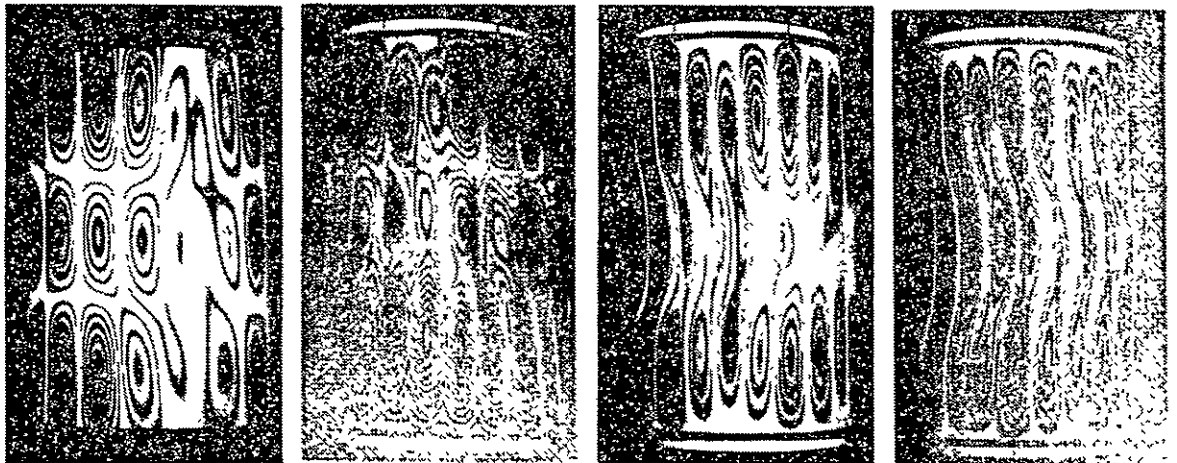


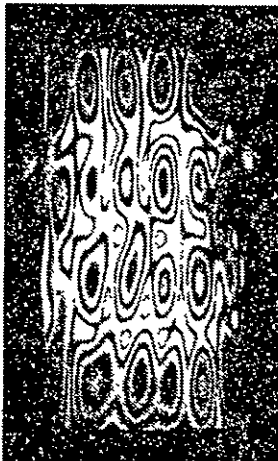
Fig. 2-8. Time-average holograms of NASA cylinder showing (1, 8), (1, 9), (cont'd.) (1, 10), (2, 5), (2, 7), and (2, ?) modes at various frequencies



(2,?) mode: (dd) 402 Hz (ee) 468 Hz (ff) 477 Hz



(3,?) mode: (gg) 440 Hz (hh) 446 Hz (ii) 504 Hz (jj) 516 Hz



(4,?) mode: (kk) 545 Hz

NOT REPRODUCIBLE

Fig. 2-8. Time-average holograms of NASA cylinder showing (2, ?), (cont'd.) (3, ?), and (4, ?) modes at various frequencies

The cylinder was excited by a 12-inch loudspeaker (with air coupling) located one foot from the cylinder and "pointed" at the cylinder. To separate two closely spaced modes, the cylinder was excited electromagnetically [Fig. 2-8 (k) and (l)].

The modes of vibration may be described in terms of (1) axial modes, in which the nodal lines are roughly circles around the cylinder, and (2) circumferential modes, in which the nodal lines are straight lines parallel to the cylindrical axis. The nodes occur in pairs. The lowest axial mode (1) has nodes at the ends. The lowest circumferential mode (2) has 4 nodes. The lowest cylinder-vibration mode, which we could not obtain, would be numbered (1, 2). To determine the number of nodes (antinodes) of a particular mode, multiply the order by 2.

Most of the modes recorded happen to be in the fundamental axial mode. We note also that many modes occur at more than one drive frequency, and in many cases the drive frequencies occur at about 2:1-ratio intervals. In particular the (1,4) mode occurs at frequencies of 52, 78, 156, 160, 322, and 422 Hz [Fig. 2-8 (d) through (i)]. Note also that 78 (e) and 156 (f), as well as 156 (f) and 322 (h), are separated by factors of two in frequency.

Similarly the (1,3) mode is noted at 104 and 209 Hz [Fig. 2-8 (a) and (b)]; the (1,5) mode at 68, 139 (and 142) and 274 Hz [Fig. 2-8 (j), (l), (m), and (n)]; the (1,7) mode at 84 and 170 Hz [Fig. 2-8 (r) and (s)]; and the (1,8) mode at 100, 200, and 410 Hz [Fig. 2-8 (t), (u), and (v)].

Harmonic distortion in the acoustic driving energy could account for this duplication of fringe patterns at driving frequencies separated by a factor of two. We did not monitor the cylinder vibrating frequency, but instrumentation to monitor the actual frequency would be useful in this respect.

Modes such as those at 370, 402, 440, and 477 Hz [Fig. 2-8 (bb), (dd), (cc) and (gg), and (ff)] are imperfect; i. e., they do not exhibit normal symmetry. This asymmetry, we feel, was caused by the cylinder being not quite perfect. In addition to the problem of making a "perfect" cylinder, we had also applied a retro-reflective coating, which probably affected the mode structure of the higher-order modes.

We also noted what appeared to be unstable modes where the cylinder seemed to be trying to vibrate in two modes simultaneously, at 118 [Fig. 2-8 (y)], 580 and 770 Hz.

Study of the photos revealed another interesting observation. On many pictures a slight fringe discontinuity or anomaly occurred at the same place on the cylinder. Inspection of the cylinder at this point revealed a barely perceptible dent. This anomaly is circled on Fig. 2-8 (u) and may be found quickly on most of the photos by casual inspection.

## 2.4 Verification of Data by Optical Interferometry

To verify that the time-average holographic interferograms give a true measure of surface displacement of vibrating objects, an optical interferometer was set up to measure the displacement. The measurement apparatus is shown in Fig. 2-9. A small mirror was fastened to the center of the 12-inch square panel and a Michelson interferometer was set up with this mirror as the movable element. The fringes were detected with a photodetector and recorded on an oscilloscope. The scope traces (Fig. 2-10) were photographed.

With the panel vibrating at the same amplitude and frequency, a time-average hologram was made. The displacement of the panel was plotted, and the displacement of the center determined by holographic interferometry was compared to the displacement measured with the optical interferometer. Figures 2-11 and 2-12 show time-average fringe patterns obtained at the same resonance frequencies but using two different driving powers.

Figures 2-13 and 2-14 show the displacement of the panel as determined from the time-average holograms. The displacement of the center as measured by the Michelson interferometer is also plotted. The error in each case is due to uncertainty in determining the exact location of the zero of the Bessel function from the hologram. The center of the panel was covered by the mirror making accuracy difficult. The error is small enough, however, to verify the time-average holographic displacement measurement.

Table 2-III

Comparison of Holographic and Optical Interferometry  
Methods for Determination of Vibration Amplitudes at  
Center of Vibrating Square Plate (microinches)

	<u>Experiment 1</u>	<u>Experiment 2</u>
Holographically	60.5 <sup>(a)</sup>	70.0 <sup>(b)</sup>
Optically	61.6 <sup>(c)</sup>	70.9 <sup>(d)</sup>
Error, %	(1.4)	(0.6)

a) from Fig. 2-11 and Table 2-I

b) from Fig. 2-12 and Table 2-I

c) from Fig. 2-10 (a)

d) from Fig. 2-10 (b), (c), (d), and (e)

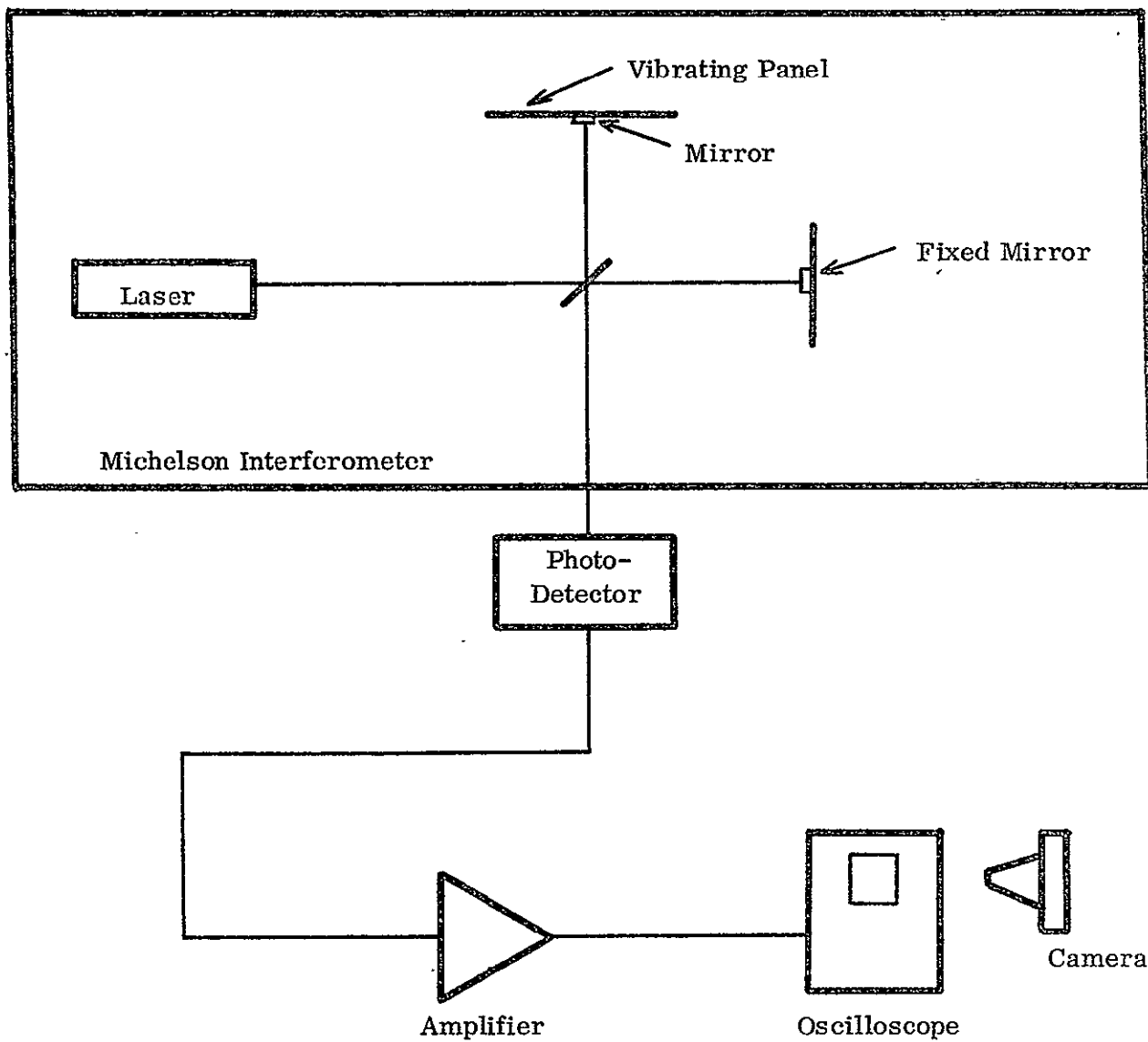
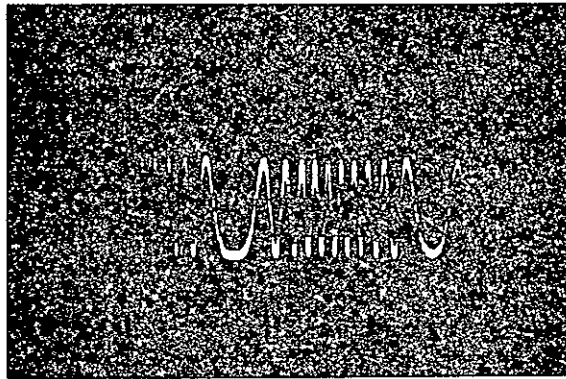
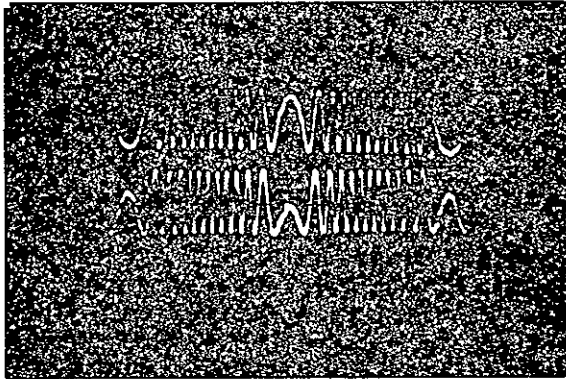


Fig. 2-9. Schematic Diagram of Optical Interferometer for Measuring Vibration Amplitude

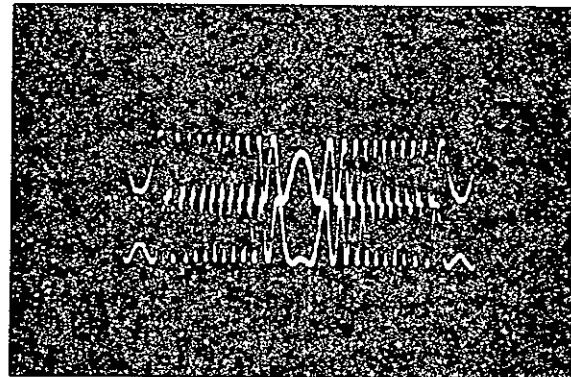


a) 9.9 fringes peak-to-peak  
(p/p)



b) 11.4 fringes p/p

c) 11.5 fringes p/p



d) 11.4 fringes p/p

e) 11.3 fringes p/p

NOT REPRODUCIBLE

Fig. 2-10. Photos of oscilloscope displays of output of optical interferometer:  
a) recorded just before hologram reconstructed in Fig. 2-11;  
b), c), d), and e) recorded before hologram reconstructed in  
Fig. 2-12

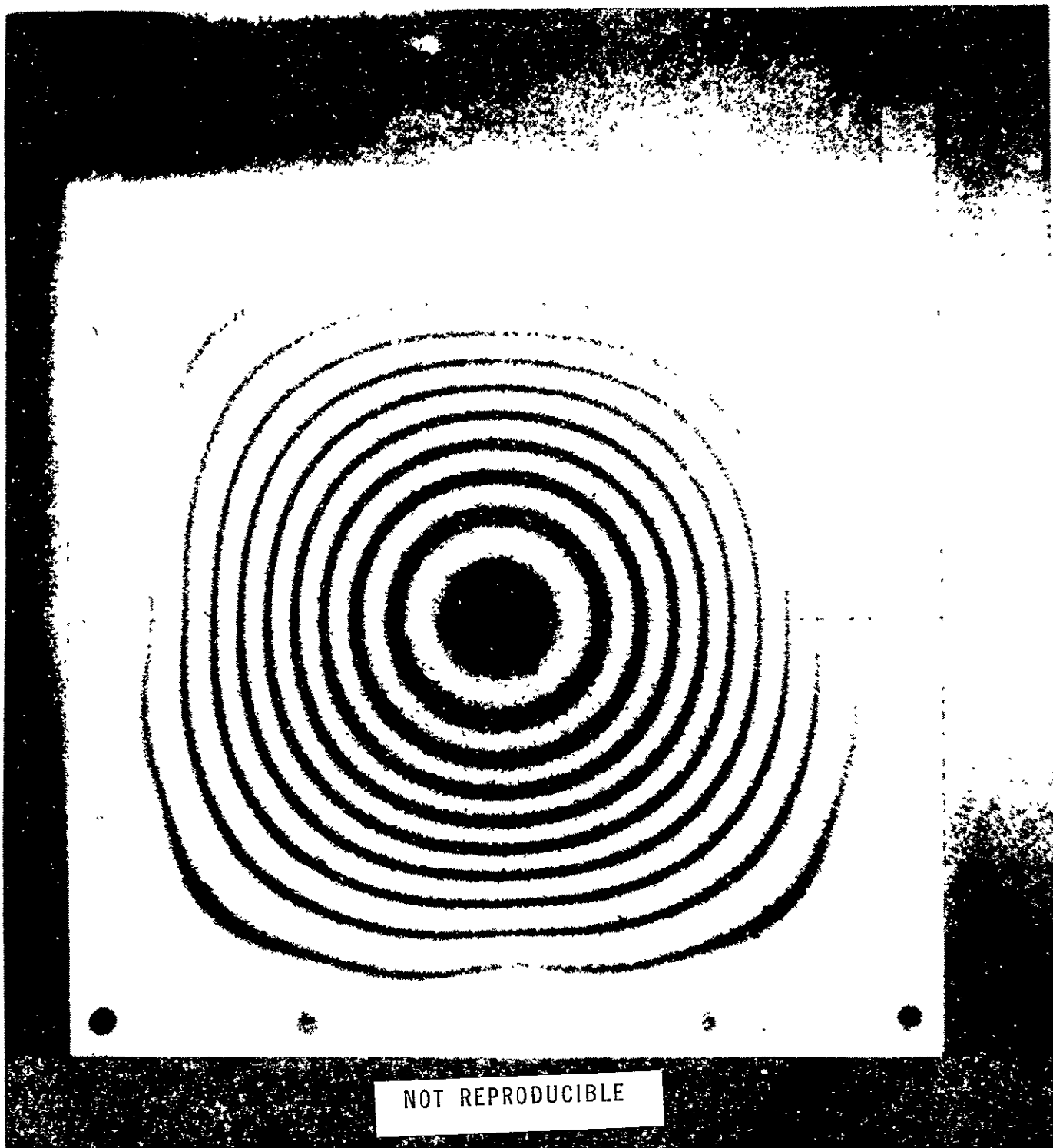


Fig. 2-11. Reconstruction of time-average hologram of vibrating square panel at fundamental frequency (205 Hz). Material is 2024 aluminum, 12" x 12" x 0.08". The center black spot is the mirror used for optical interferometry, covered with tape during holographic exposure. Amplitude at center, measured optically is  $61.6 \mu$  inches; holographically it is  $60.5 \mu$  inches.

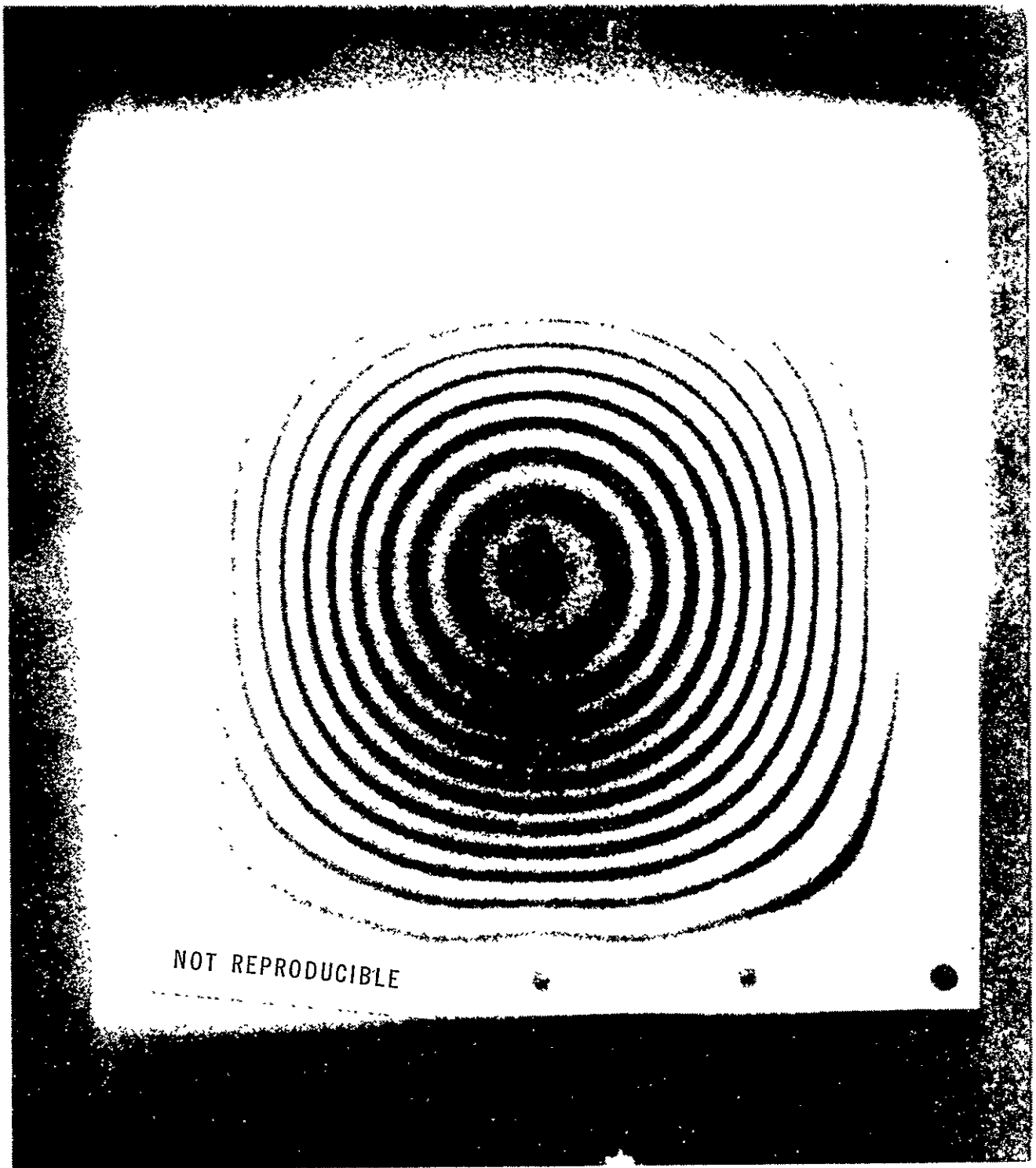


Fig. 2-12. Reconstruction of time-average holographic interferogram of square panel, vibrating at fundamental frequency (205 Hz) but driven with slightly higher power than during recording of Fig. 2-11. Amplitude at center, measured optically is  $70.9 \mu$  inches; holographically it is  $70.0 \mu$  inches.



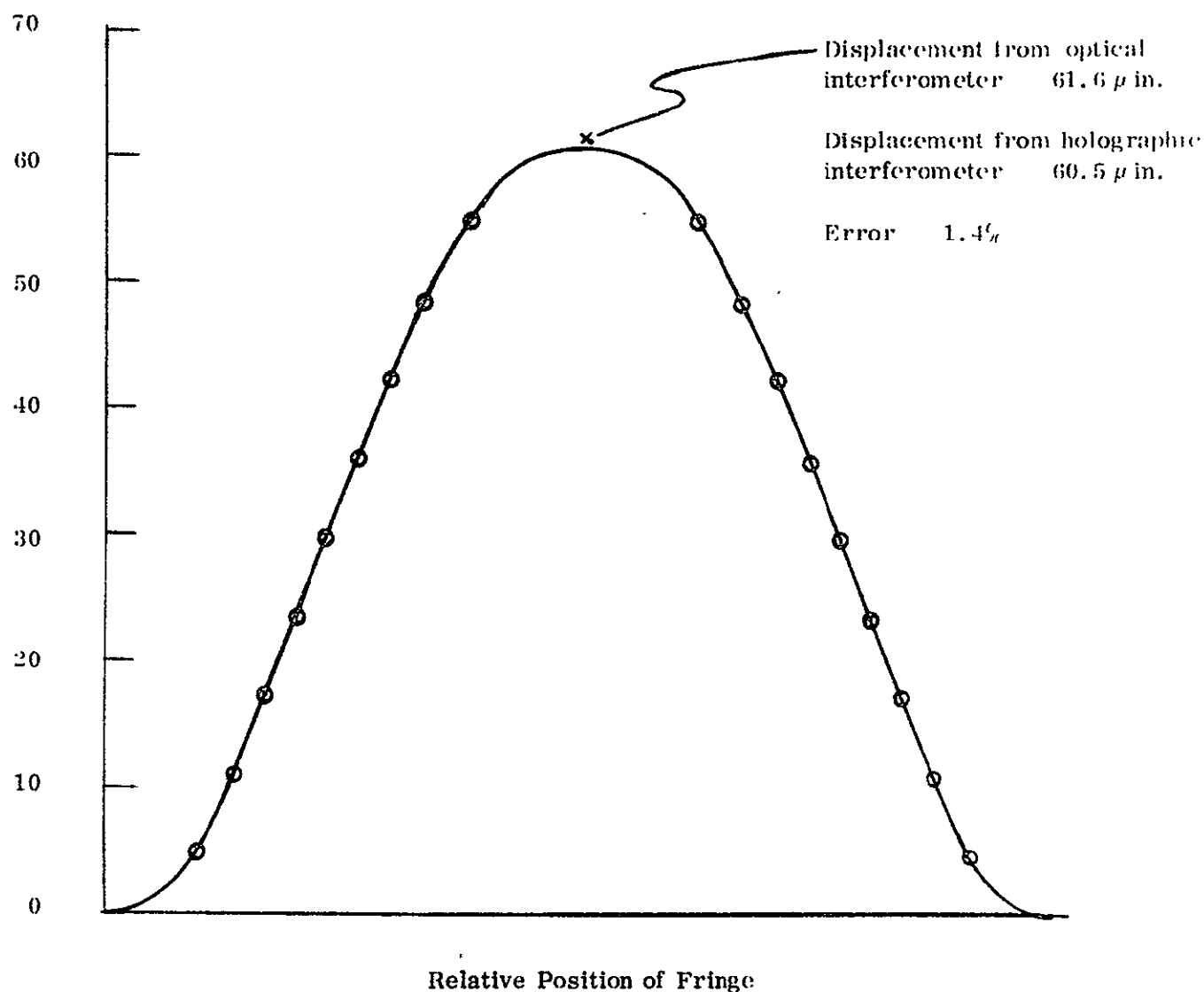


Fig. 2-13. Vibration-amplitude displacement, determined by holographic interferometry (from Fig. 2-11 and Table 2-1) versus fringe position of a vibrating square aluminum plate

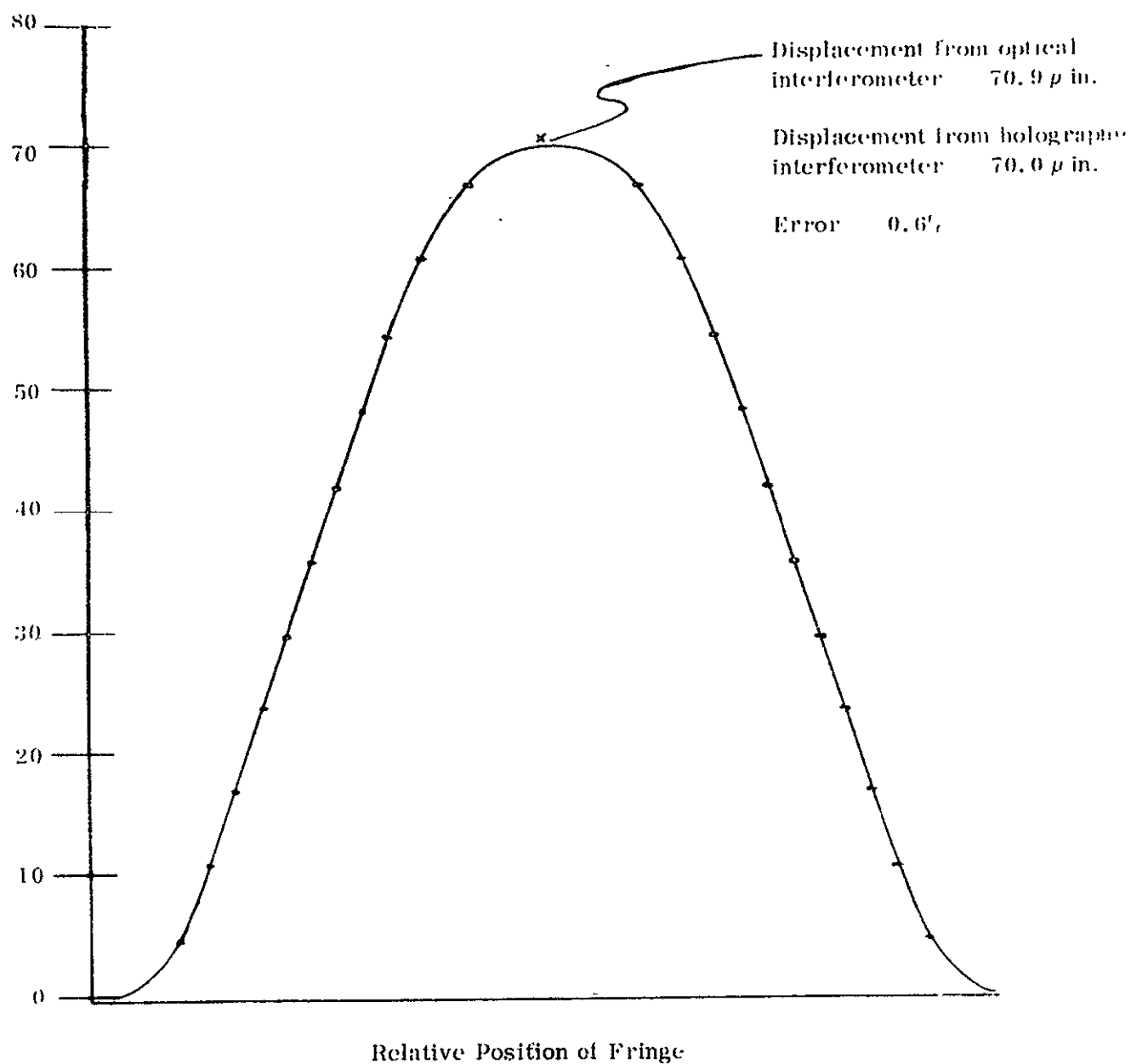


Fig. 2-14. Vibration-amplitude displacement, determined by holographic interferometry (from Fig. 2-12 and Table 2-1) versus fringe position of a vibrating aluminum plate

## 2.5 Application Limitations

Important limitations to consider in the application of time-average holographic interferometry include displacement-amplitude measurement limits, maximum and minimum amplitude limits, vibration-frequency limitations, and measurable area limitations.

### 2.5.1 Displacement-Amplitude Accuracy Limits

The displacement amplitude at the  $n^{\text{th}}$ -null fringe of the characteristic zero-order Bessel function is given by the expression:

$$\delta m_n = \frac{\rho_n \lambda}{2 \pi (\cos \Theta_1 + \cos \Theta_2)} \quad (2-11)$$

where

$\delta m_n$  = displacement (zero-to-peak amplitude) at  $n^{\text{th}}$  dark fringe,

$\rho_n$  =  $n^{\text{th}}$  root of the zero-order Bessel function,

$\lambda$  = wavelength of the laser light, and

$(\cos \Theta_1 + \cos \Theta_2)$  = obliquity factor.

The accuracy of  $m_n$  depends only on the accuracy of  $(\cos \Theta_1 + \cos \Theta_2)$ , if the zero position is known exactly. Because the position of the  $n^{\text{th}}$  zero can be measured only to within 10 percent of the fringe spacing for visual observation and to about 1 percent using microdensitometer techniques, there is a corresponding uncertainty in  $m_n$ .

The uncertainty ( $\delta m_n$ ) in the value of the displacement  $m_n$  due to position uncertainty is therefore:

$$\delta m_n = \frac{\lambda}{2 \pi (\cos \Theta_1 + \cos \Theta_2)} \frac{(\rho_{n+1} - \rho_n)}{C} \quad (2-12)$$

where the factor, C, is 10 for visual observation and 100 for microdensitometer techniques.

For  $n \geq 2$ , the phase change between adjacent fringes is approximately  $\pi = (\rho_{n+1} - \rho_n)$ . Thus,  $\delta m_n$  is given by the equation:

$$\delta m_n = \frac{\lambda}{2 (\cos \Theta_1 + \cos \Theta_2) C} \quad (2-13)$$

For  $(\cos \Theta_1 + \cos \Theta_2) = 2$ , the accuracy of  $\delta m_n$  is  $\lambda/40$  (12.2 nm) for  $\lambda = 488.0$  nm for visual determinations and  $\lambda/400$  (1.22 nm) for microdensitometer determinations. The change in displacement between adjacent fringes is correspondingly  $\lambda/4$  (122 nm).

### 2.5.2 Maximum-Amplitude Limit

The maximum displacement amplitudes that can be measured by use of time-average holography depend on the maximum resolvable fringe spatial frequency.

The fringe spatial frequency ( $f_n$ ) is determined by the following equation:

$$f_n = \frac{1}{\Delta x_n} = \frac{S}{\Delta m_n}, \quad (2-14)$$

where:

$\Delta x_n$  = the fringe spacing,

$$\Delta m_n = \frac{\lambda (\rho_{n+1} - \rho_n)}{2 \pi (\cos \Theta_1 + \cos \Theta_2)} \approx \frac{\lambda}{2 (\cos \Theta_1 + \cos \Theta_2)},$$

which is the displacement amplitude between the  $n^{\text{th}}$  and  $(n+1)^{\text{th}}$  fringe, and

$S = \Delta m_n / \Delta x_n$ , is the slope (rate of change of displacement amplitude with respect to position coordinate) of the object compared to its static condition.

Assuming  $(\cos \Theta_1 + \cos \Theta_2) = 2$ , the fringe spatial frequency is  $f_n = \frac{4S}{\lambda}$ .

A fringe spatial frequency of 4 fringes per millimeter has been observed experimentally. This frequency corresponds to a maximum object slope of:

$$\begin{aligned} S = f_n \Delta m_n &= \left( \frac{4 \text{ fringes}}{\text{mm}} \right) \left( \frac{122 \text{ nm}}{\text{fringe}} \right) \\ &= 488 \text{ nm/mm.} \end{aligned} \quad (2-15)$$

Maximum measurable displacement amplitudes may be estimated as follows.

Assume that a 20-inch-long panel is vibrating with displacement  $[m(x)]$  according to the equation:

$$m(x) = M \sin\left(\frac{n\pi x}{\ell}\right) \quad (2-16)$$

where

$m(x)$  = one-dimensional amplitude distribution.

$\ell$  = 20 inches, the length of the object along the  $x$  coordinate,

$n = 1, 2, \dots$  defines the mode of vibration, and

$M$  = maximum displacement amplitude.

The maximum slope,  $S = dm/dx$ , occurs when the displacement is zero and is given by:

$$S = \frac{n\pi M}{\ell} \quad , \quad (2-17)$$

and the maximum displacement amplitude is given by:

$$M = \frac{S\ell}{n\pi} \quad . \quad (2-18)$$

Assuming that  $n = 1$ ,  $\ell = 20$  inches, and  $S = 0.488 \times 10^{-3}$ , the maximum displacement amplitude is about 0.01 inch or 0.25 mm.

### 2.5.3 Minimum-Amplitude Limit

To determine small displacement amplitudes, those points on the object having maximum amplitudes must be displaced sufficiently so that the  $J_0^2$  function passes through its first zero to establish a reference percentage modulation from which displacement amplitudes for intermediate points can be determined with a photodensitometer.

Accordingly there must be at least one dark fringe in the reconstructed interferogram. Points on the object having a displacement amplitude of  $0.2 \lambda$ , or about 100 nanometers, can then be immediately determined by the eye.

The accuracy with which intermediate-point displacement can be determined depends on such factors as the degree of fringe contrast and object-illumination uniformity. In general, carefully controlled experimental techniques permit a determination of minimum amplitudes of about 10 nanometers.

### 2.5.4 Vibration-Frequency Limitations

The only vibration-frequency limitation in the case of an object vibrating under steady-state excitation is at very low frequencies where the vibration period begins to approach the duration of the exposure time. Under these conditions it can be shown that the expression for the intensity ratio contains additional terms to the  $J_0(\rho)$  term of the form  $J_1(\rho)$ ,  $J_2(\rho) \dots J_{n-1}(\rho)$ .

Thus, fringe interpretation can be complicated at very low frequencies. However, the problem is easily overcome by reducing the intensity of the light striking the emulsion during exposure and increasing the exposure time until it becomes much greater than the vibration period.

High-frequency limitations result from the nature of the object under consideration, limitations in available driving transducers, and associated energy-coupling problems at high frequencies.

GCO is extensively engaged in the application of holographic interferometry as a nondestructive testing technique in the detection of flaws in sub-surface bonds. The types of bonds examined have included beryllium-to-steel, steel-to-steel, aluminum-to-aluminum, and titanium-to-titanium. The frequencies used in this technique have ranged from 60 Hz to 250 kHz. Frequencies in the audible and low-ultrasonic ranges present no problem to the time-average holographic interferometric technique.

#### 2.5.5 Measurable-Area Limitations

The maximum area that can be inspected holographically at any one time is determined by the environmental stability.

As the area to be inspected increases it is necessary to increase the object-to-hologram distance proportionately. With increase in object-to-hologram distance the system becomes more sensitive to index-of-refraction variations in the air. When refractive-index variation becomes a problem, it can be solved by close control of ambient conditions, if the distances and exposures are not too long.

The maximum allowable vibration amplitude also decreases as object-to-hologram distance increases because the resolvable spatial frequency of the interferometric fringes decreases.

With these limitations in mind, let us consider the maximum area that can be holographed. Holograms of the 18-inch-diameter NASA test cylinder, which has a viewable area of nearly 4 square feet, have been recorded in 0.6 second on Kodak 649F film.

Consider the maximum size from just a time basis. Holograms requiring nearly an hour for exposure have been recorded. They are very difficult to obtain because of the problem of maintaining position and pathlength stability. A more reasonable and practical maximum exposure time would be about one minute. By using Agfa 10E56 holographic plates (10 times faster than 649F), a more powerful argon laser (4 times the power of the CRL Model 52 laser), and one-minute exposure (100 times longer), the area could be increased by a factor of  $10 \times 4 \times 100 = 4000$  or from 4 to 16,000 square feet.

We have, however, neglected spherical spreading losses due to increased object distance. The change in exposure caused by spherical spreading losses in this case would be proportional to  $\left(\frac{z' - z}{z}\right)^2$ , where:

$z'$  = projected increased object distance, and  
 $z$  = original object distance.

Normally the change would be proportional to the fourth power, but use of retro-reflective coating makes the object behave somewhat like a giant corner reflector

reflecting all energy back, except for a spherical spreading loss proportional to the square of the distance.

We also use the rule of thumb that the distance,  $z$ , from hologram to object must be three times the maximum dimension,  $D$ , of the object or  $z = 3D$ . This rule permits certain simplifying assumptions in calculating the obliquity factor. For these rough calculations we let the area,  $A$ , to be holographed equal  $D^2$ . We can also say that increased loss due to spherical spreading can be expressed as  $(\frac{D' - D}{D})^2$ . Taking all these factors into account, the extrapolated area  $[A' = (D')^2]$  that can be holographed, based on our experimental data ( $A = D^2$ ), is:

$$(D')^2 = \frac{(D)^2 (\text{Film Factor}) (\text{Laser-Power Factor}) (\text{Time Factor})}{(\frac{D' - D}{D})^2}$$

Assume:

$$\begin{aligned} D' &\gg D \\ \text{approximately } (\frac{D' - D}{D})^2 &= (\frac{D'}{D})^2 \\ (D')^4 &= D^4 (\text{Film Factor}) (\text{Laser-Power Factor}) (\text{Time Factor}) \\ (D')^2 &= A' \\ &= A [ (\text{Film Factor}) (\text{Laser-Power Factor}) (\text{Time Factor}) ]^{1/2} \\ D' &= D [ (\text{Film Factor}) (\text{Laser-Power Factor}) (\text{Time Factor}) ]^{1/4} \end{aligned}$$

Using the numbers above:

$$\begin{aligned} A' &= (4 \text{ ft.}^2) [ (10) (4) (100) ]^{1/2} = 250 \text{ sq. ft.} \\ D' &= 2 \text{ ft.} [4000]^{1/4} = 16 \text{ ft.} \end{aligned}$$

Thus, if we used a CRL 53 laser instead of a CRL Model 52, Agfa 10E56 plates instead of Kodak 649F, and allowed an exposure of 1 minute instead of 0.6 second, then we estimate that we could readily holograph an area of 250 square feet, or about a 16-foot square.

### 3.0 PHASE-SHIFTED REFERENCE BEAM

#### 3.1 Theory

Two approaches to phase measurement were considered. In one approach, the phase of the reference wavefront was varied with respect to that of the object wavefront to shift the apparent node on the vibrating object. This approach was used with both time-average and real-time techniques. The other approach was the use of a shuttered laser system to strobe the illumination and reference beams and "freeze" the fringe motion. The strobing device was synchronously driven by the oscillator that drove the panel. A phase-shifting network was used to vary the relative phase between the object and illumination.

A hologram is a record on film of the interference-fringe pattern that occurs when mutually coherent reference and object wavefronts combine. If the phase of either wave (or both) is time-variant, then the phase of the interference pattern is also usually time-variant. Time variance results in a movement of the pattern and hence a reduced contrast of the recorded fringes following the exposure integration.

To illustrate these time-varying effects we may assume that the fields of the reference and object wavefronts at the holograph plane are given by:

$$E_H(t) = E_r \exp\{j[f_r(t)]\} + E_o \exp\{j[f_o(t)]\} , \quad (3-1)$$

(Note that E denotes the field,  $\exp[j\frac{2\pi ct}{\lambda}]$ .) The exponential always cancels for coherent fields when we detect them, since we can only detect intensity. Then the intensity in the hologram plane may be represented as:

$$I = |E_r|^2 + |E_o|^2 + 2\text{Re}[E_r E_o^*] \cos [f_r(t) - f_o(t)] . \quad (3-2)$$

Assume that the phases of both waves have a sinusoidal dependence at a radian frequency of  $\omega$ . Then:

$$\begin{aligned} f_r(t) &= k \Delta_r \sin (\omega t + \phi_r) \\ \text{and} \\ f_o(t) &= k \Delta_o \sin (\omega t + \phi_o) , \end{aligned} \quad (3-3)$$

where  $k \Delta_r$  and  $k \Delta_o$  are the amplitudes of the time-variant phases of the reference and object waves, respectively, ( $k = 2\pi/\lambda$  is the propagation constant for the light used), and  $\phi_r$  and  $\phi_o$  are the time-variant phases of the reference and object waves, respectively.



The phase of the cosine interference fringes (3-2) then becomes:

$$f_r(t) - f_o(t) = k\Delta_r \sin(\omega t + \phi_r) - k\Delta_o \sin(\omega t + \phi_s) \quad (3-4)$$

which may be written more simply as:

$$f_r(t) - f_o(t) = k\chi \sin(\omega t), \quad (3-5)$$

where

$$\chi = \sqrt{\Delta_r^2 + \Delta_o^2 - 2\Delta_r\Delta_o \cos \phi}, \text{ and}$$

$$\phi = \text{phase difference between } f_r(t) \text{ and } f_o(t)$$

The term  $k\chi$  is the magnitude of the resultant phasor formed by the addition of two phasors representing the reference- and object-wave phase variations.

Inserting the phase equivalence (3-5) into the intensity expression (3-2) gives:

$$I = |E_r|^2 + |E_o|^2 + 2 \operatorname{Re} [E_r E_o^*] \cos [k\chi \sin(\omega t)]. \quad (3-6)$$

Integrating over a time,  $T$ , which includes many cycles at the frequency,  $\omega/2\pi$ , gives an exposure:

$$\langle I \rangle T = T [ |E_o|^2 + |E_r|^2 + 2 \operatorname{Re} (E_o E_r^*) J_0(k\chi) ]. \quad (3-7)$$

Since the amplitude of the reconstructed wave is proportional to the exposure variation, this wave amplitude is now modified at each point of the hologram by  $J_0(k\chi)$ , which is the usual result for time-average holography except for the more complex nature of  $\chi$  in the present derivation.

In real-time interferometry, the vibrating-object wavefront is superimposed over a wavefront reconstructed from a hologram of the static object. The wave from the vibrating object may be written as:

$$E_o \exp [j f_o(t)]. \quad (3-8)$$

If the hologram is reconstructed with a wave whose phase varies sinusoidally with time, the reconstructed wave may be written:

$$E'_o(t) = aE_o \exp [j f_r(t)], \quad (3-9)$$

where  $a$  is a constant that involves the holographic recording and reconstruction processes and that can be varied by adjusting the power in the reconstructing wave.

To obtain fringes with the highest contrast the amplitudes of the two waves are made equal ( $a = 1$ ); the resulting intensity from the sum of the two waves is:

$$I = 2|E_o|^2 \{1 + \cos [f_o(t) - f_r(t)]\} \quad (3-10)$$

If the object is vibrating at the same frequency,  $\omega$ , as the sinusoidal phase variation of the hologram-reconstructing wave, the phase terms of the waves may be written as

$$f_o(t) = \alpha + k\Delta_o \sin \omega t$$

and

$$f_r(t) = \beta + k\Delta_r \sin (\omega t + \phi) , \quad (3-11)$$

where  $\alpha$  is the static phase caused by change in either the object or object illumination; and  $\beta$  similarly represents changes in reference wavefront or hologram position. When the object and reconstructed object wavefronts are combined, the resulting static fringe system is determined by  $\alpha - \beta = \phi_\epsilon$ . Observation of the resulting wavefront with a detector (such as the eye) having an integrating time constant,  $T \gg 2\pi/\omega$ , gives an average intensity:

$$\langle I \rangle = 2|E_o|^2 [1 + J_o(k\lambda) \cos (\phi_\epsilon)] \quad (3-12)$$

where  $\lambda$  is the magnitude of the phasor formed by adding two phasors representing the phase variation of the real-time and reconstructed object wavefronts. The  $J_o$  term is from vibration, and  $\cos \phi_\epsilon$  is from the static fringe system. When image and object are in perfect phase registration, equation (3-12) may be written as:

$$\langle I \rangle = 2|E_o|^2 [1 + J_o(k\lambda)] . \quad (3-13)$$

### 3.1.1 Argument of the Bessel Function

For both time-average holography and real-time holographic interferometry, it has been shown that if the reference phase is sinusoidally altered at the frequency of the vibrating object, the expression representing the intensity of the observed wave is identical to the usual expression, except that the argument of the Bessel amplitude-weighting function is more complex, being dependent on both the object motion and the reference-phase shift. This Bessel function describes the apparent brightness of any point of the object, and hence, the appearance of the fringes over the surface of the object. Since the interpretation of these fringes gives the desired information in these two techniques, it is important to analyze the Bessel function argument and to understand the effect of varying the parameters of that argument.

For the sake of clarity, the following discussion is limited to real-time holographic interferometry, but the derivation is equally valid for the Bessel function of time-average holography.

The argument to be considered is a function of the difference between the object- and reference-wave phase shifts. A phasor plot provides a good visualization of this difference, since both terms vary at the same radian frequency. Only the magnitude of the resultant phasor is required, since the phase is lost in the time integration over many cycles. Concentric circles around the origin of the phasor diagram indicate the loci of constant Bessel arguments. Figure 3-1 shows a typical case where  $k\Delta_r = 3\pi$ ,  $\phi_r = 30^\circ$ ,  $k\Delta_o = 2.5\pi$ , and  $\phi_o = 60^\circ$ . The resultant phasor has a magnitude of  $1.5\pi$ . Applying the law of cosines to the phasor triangle gives the magnitude of the resultant phasor as:

$$k\chi = k [\Delta_r^2 + \Delta_o^2 - 2\Delta_r \Delta_o \cos(\phi_r - \phi_o)]^{1/2} \quad (3-14)$$

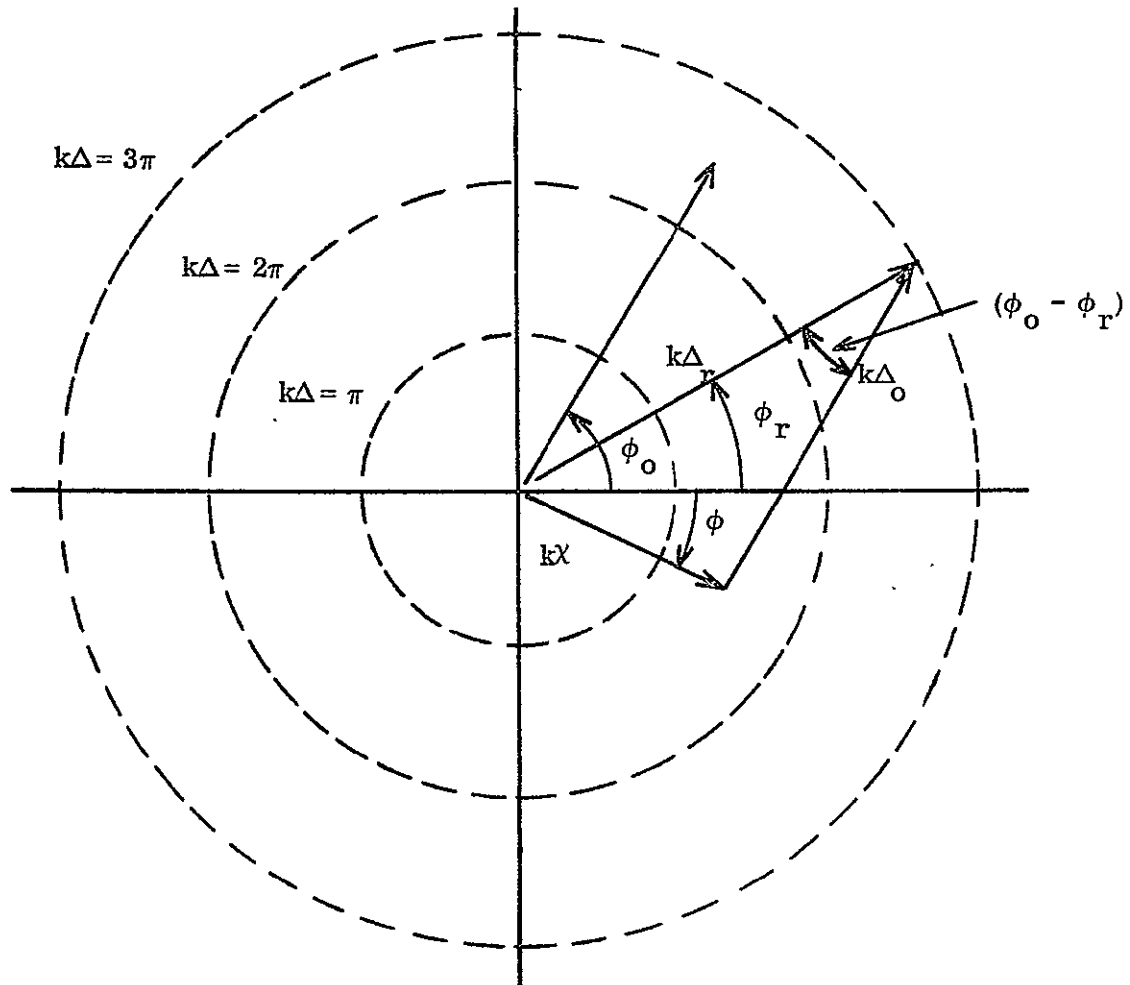


Fig. 3-1. Phasor diagram showing object- and reference-wave phasors yielding resultant phasor with magnitude  $k\chi$

It is now assumed that over a local region of interest all object points have the same phase. Also, this phase of the object wave is assumed to be zero (arbitrary choice of phase reference).

Figure 3-2 shows phasors for several object points (1, 2, and 3) moving with the same phase ( $0^\circ$ ) but different magnitudes and a reference phasor lagging the object by  $\phi_r$ . The resultant phasors,  $k\chi_n$ , are shown and indicate that the smallest Bessel argument for the three points is that for point 2. In fact, it can be seen from the figure that for the reference-wave magnitude and phase shown, any object point with zero phase and a magnitude different from  $k\Delta^2$  has a resultant with magnitude larger than that for point 2. Therefore, the argument has a relative minimum at points with this magnitude and phase of motion. If this minimum argument is small enough (say  $k\chi < 1.6$  radians), the Bessel function and the corresponding object brightness are absolute maximums for such points.

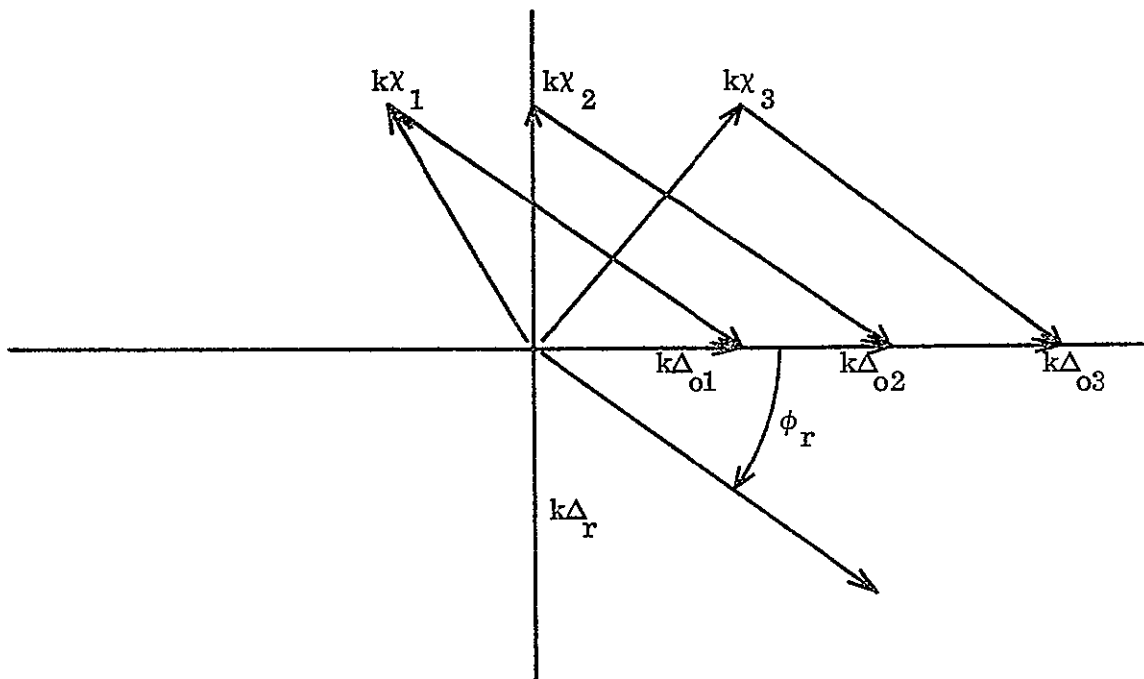


Fig. 3-2. Phasor diagram for three object points, showing that the minimum phasor resultant is for point 2

From Fig. 3-2 it can be observed that only the co-phase component of the reference-wave phase shift can be instrumental in reducing the argument of the Bessel function, while the quadrature component always increases the argument and puts a lower limit on its magnitude. The object points that have a minimum

Bessel argument are those with a phase-shift magnitude that matches the co-phase component of the reference-wave shift.

### 3.2 Application of Phase-Shifted Reference Beam

In the usual cases of time-average holography and real-time holographic interferometry, the Bessel function argument is a function of the object-phase-shift magnitude only (set  $\Delta_r = 0$  in Eq. 3-14). By studying the zeros and relative maximums of this "brightness coefficient" the magnitude of the vibration may be determined for various points of the object, but it is not possible to determine the phase of the vibration of object points.

If, however, the reference wave is phase-shifted at the same frequency as the object vibration, the Bessel argument also becomes a function of the object phase,  $\phi_o$ , as shown by Eq. 3-14. It may be possible then to determine the phase by studying the resulting fringes on the object. The problem is how to separate the effect of the object phase from the effects of the other parameters.

Assume that the object is vibrating sinusoidally and that an electrical signal at the frequency of this vibration is available (this signal may come either from electronics used to drive the object or from a detector that senses the object motion). Further assume that this signal is passed through a variable-gain device and a variable phase-shifter before being applied to a device that phase-shifts the reference beam. The operator now has the ability to independently alter the magnitude,  $k\Delta_r$ , of the reference-phase shift and the phase,  $\phi_r$ , of this shift relative to the object. For now, it is assumed that the magnitude control is not calibrated and that while the phase control is divided into degrees of phase shift, the control position for object and reference shifts in-phase ( $\phi_o - \phi_r = 0$ ) is not known.

The general technique for determining the relative phase is described below, followed by two other possibilities for special cases. In the following discussion, real-time holographic interferometry is assumed, since the operator can easily determine the effect of a parameter change. Furthermore, the technique is equally valid for time-average holography if time is available to process the holograms for each parameter change.

#### 3.2.1 General Technique (Variable-Phase Shift, Constant Magnitude of Reference Wave)

The main technique consists of varying the phase shift of the reference wave while holding the magnitude constant. The operator first sets in some small reference magnitude,  $k\Delta_r$ . In general, this operation causes the brightest region to move off the vibrational node of the object and to form an interferometric node elsewhere on the object. If the relative phase happens to be at  $\phi_o - \phi_r = 90^\circ$  or  $270^\circ$ , however, the brightest region does not move from the vibrational node but decreases

in brightness. If the bright spot dims instead of moving, the operator turns the phase control about  $90^\circ$  (to  $0^\circ$  or  $180^\circ$ ) and then increases the magnitude from zero to move the brightest region off the vibrational node.

The operator then leaves the magnitude constant and adjusts the phase. As the phase is changed, the interferometric node (brightest region) moves across the object. As the phase control is rotated in one direction, at some phase the interferometric node stops and reverses. When this reversal occurs, the relative phase between the object and the reference waves is passing through zero. Comparing the phase-dial reading of this point with readings for other points allows a determination of relative phase between the object points.

The above technique can be illustrated by the phasor diagram in Fig. 3-3. The circle is the locus of all reference-wave phasors having the constant magnitude chosen by the operator. Several reference-wave phasors (1-4) are shown with the corresponding object-wave phasors that give a minimum Bessel argument in each case. (Recall that the phase of object-wave phasors was assumed constant and zero.) Note that as the reference-wave phase approaches zero, the interferometric node moves to object points with increasing phasor magnitudes (i. e., points farther from the vibrational node). Also notice that as the reference-wave phase approaches zero, the interferometric node increases in brightness until it is as bright as a vibrational node in the usual fixed-reference case (Bessel argument equal to zero).

The case illustrated in Fig. 3-3 assumes that for each reference-wave phase there is an object-wave phasor that causes the resultant to lie along the vertical axis.

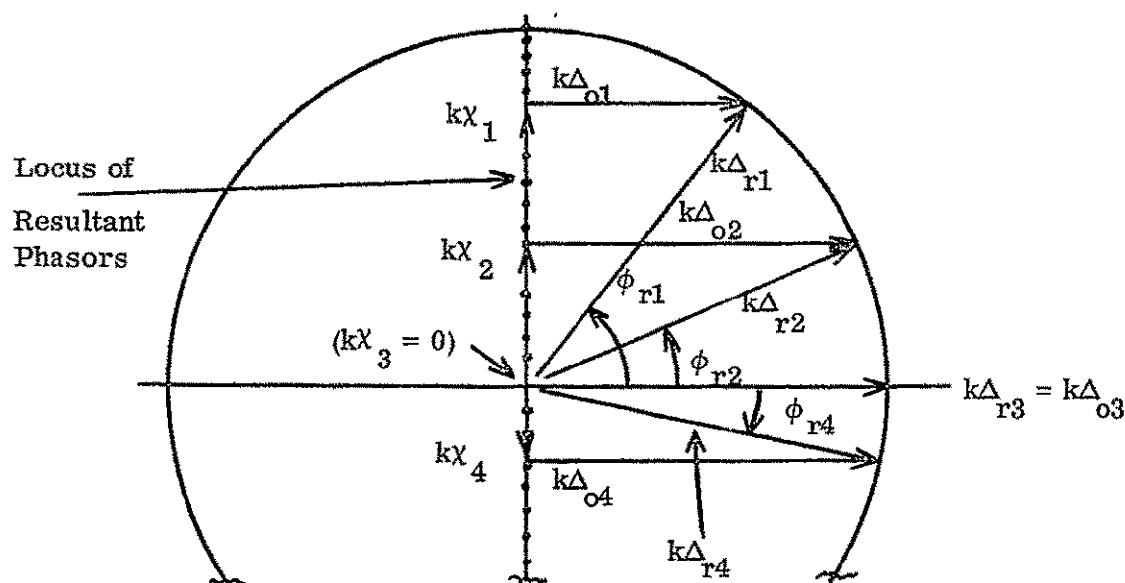


Fig. 3-3. Phasor diagram showing effect of reference-wave phase variation at constant magnitude

If the magnitude of the reference-wave phase shift is made greater than that of the object-wave phase shift for the antinodal point, however, the locus of resultant phasors is as shown in Fig. 3-3. It is seen that the effect on the fringes is similar for the phase control near  $90^\circ$ .

As the phase approaches zero, the interferometric node moves away from the vibrational node until it reaches the antinode. Since there is then no further motion of the interferometric node, it is now necessary to determine the zero phase by the brightness (which increases as zero phase is approached) of the antinode or by motion of other relative maxima or minima of the Bessel function. It is, therefore, desirable to keep the reference-wave-shift magnitude smaller than the largest object-wave phase shift, yet it is wise to make the reference-wave shift as large as possible to maximize the interferometric-node motion for a given phase shift and hence to increase the phase resolution.

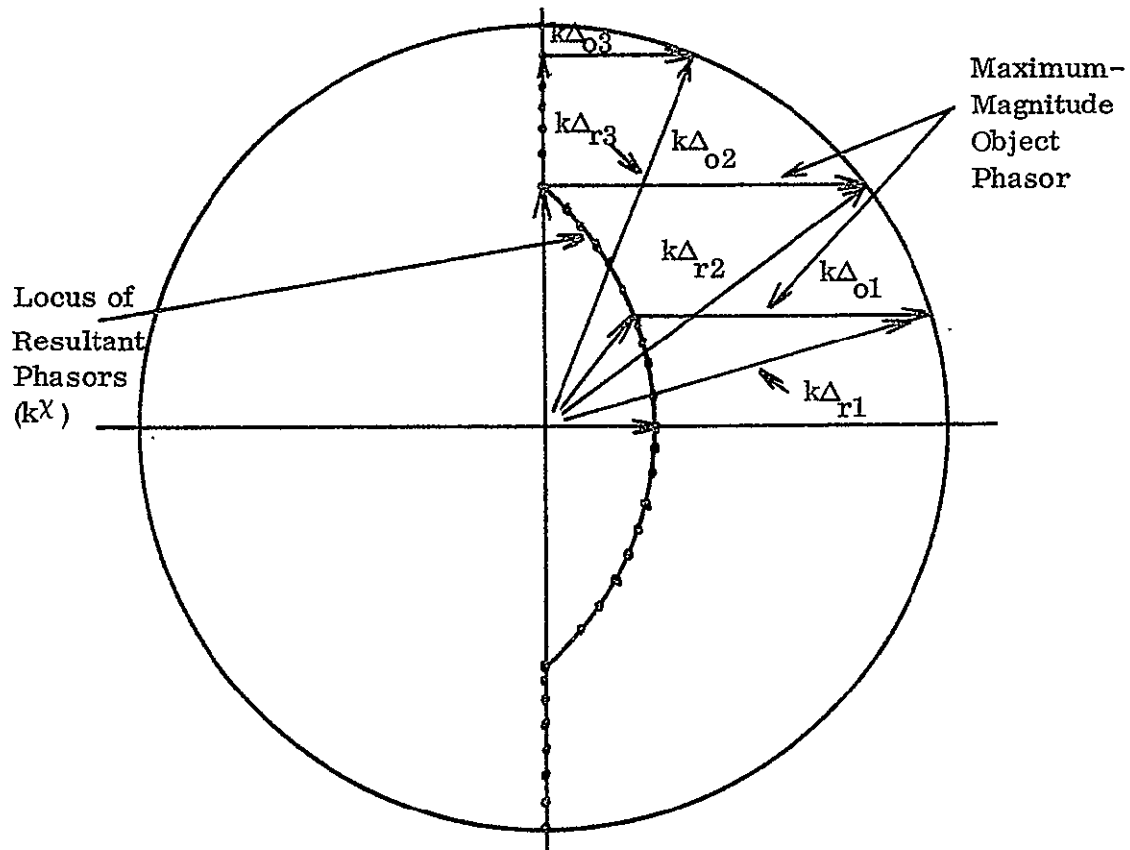


Fig. 3-4. Phasor diagram showing effect of reference-wave phase shift with excessive magnitude

### 3.2.2 Case of Only Two Object-Wave Phases

If the vibrating object is such that only two object-wave phases ( $0^\circ$  and  $180^\circ$ ) can be assumed to exist, then all regions of the same phase may be found in the following manner. During observation of the real-time fringes, a small phase shift is added to the reference wave. The magnitude and phase are not important (so long as the  $90^\circ$  case mentioned above is avoided). The bright regions normally located on the vibrational nodes would move toward some of the anti-nodes and away from others. Labeling all those areas into which the interferometric nodes moved as "plus" and those from which they have moved as "minus" completes the phase determination in this simple case.

### 3.2.3 Magnitude-Control Calibration of Reference-Wave Phase Shifter

The remaining technique to be considered requires calibration of the magnitude control of the reference phase shifter. The operator begins by observing the usual real-time fringes with no reference shift. The magnitude of the motion is determined in the usual manner by counting fringes from a vibrational node to an object point of interest. This magnitude is then set into the reference control, thus making  $k\Delta_r = k\Delta_o$  for the point of interest. The phase control is then rotated until the point of interest is centered in the interferometric node. The reading on the phase dial is then noted and compared to readings obtained for other points by the same means.

### 3.2.4 Objects with Continuous Phase Variation

In the above discussions, it is assumed that the phase of vibration is constant for all object points considered. In many cases the vibration phase varies continuously over the object. A common example occurs when a structure is driven at a frequency in the region of two closely spaced resonant modes. In these cases, it is important to make sure that the interferometric node reverses its direction at the point of interest. This reversal may be accomplished by proper adjustment of the magnitude control while sweeping the phase control back and forth through the setting that causes the interferometric node to stop and reverse.

A system with calibrated reference-magnitude control would be very useful in this case. The operator sets the control to zero and counts the number of fringes between a vibrational node and the point of interest. He then sets this value into the control, making magnitude of the reference-wave phase shift match the object point. Turning the phase control until the interferometric node is centered on the point of interest completes the measurement. A check is available since the node should just reach the point before reversing its motion. It should be noted that the interferometric node does not represent a locus of points with either equal phase or equal magnitude.

To accomplish the phase shift, one of the reference mirrors,  $M_2$ , is replaced with a mirror mounted on a piezoelectric mount. The motion of this mirror ( $M_{pz}$ )



is normal to the mirror surface. The piezoelectric mount is driven in synchronism with the acoustic driver, which is vibrating the panel. The signal to the mirror may be phase shifted continuously over  $360^\circ$  relative to the acoustic driver. A diagram of the holographic setup is shown in Fig. 3-5 and the mirror is shown in Fig. 3-6.

### 3.3 Experimental Verification of Phase-Shifted Reference-Beam Method

Phase measurement by the phase-shifted reference-beam method was verified by experiments on an edge-clamped aluminum plate, 0.080-inch thick, 12-inches square, and excited acoustically by a 12-inch speaker. The reference beam was phase shifted by a mirror mounted on a piezoelectric device to alter the reference-wave pathlength. The amplifiers driving the speaker and the piezoelectric transducer were controlled from a Hewlett-Packard Model 203A Oscillator. This oscillator provides two variable-amplitude sine-wave outputs with an adjustable phase shift between the two. The actual phase of the moving reference-beam mirror was obtained by using a photodetector to observe fringes in an interferometer that has the reference mirror as one of its elements. The phase of the object was determined by "strobing" the laser with an electro-optic modulator. A maximum number of real-time fringes between a node and an antinode indicated that the shutter was being opened when the object was at its maximum displacement,  $\omega t = \pi/2 (2n - 1)$ . The light for hologram formation and reconstruction was from an argon laser at a wavelength of 514.5 nm. Hologram exposure time was 1.5 seconds, and Kodak 649F spectroscopic plates were used.

Figure 3-7 shows photographs of time-average hologram reconstructions to illustrate the effects of various reference-wave vibration magnitudes and phases. The aluminum plate was vibrating in its (1, 2) mode at a frequency of 1165 Hz. The left column shows the effect of changing the vibration magnitude while holding the relative phase equal. In the photograph at the top of this column the magnitude has been increased to approximately that of the object antinodes. The top row of pictures shows the effect of varying the phase while holding the magnitude constant. The first and last pictures of this row show vividly the ability to distinguish between regions vibrating with "plus" ( $0^\circ$ ) phase and with "minus" ( $180^\circ$ ) phase.

The center column shows the effect of varying the magnitude with the relative phase constant at  $90^\circ$ . As the magnitude increases, the fringe contrast reduces, but there is very little shifting of the fringes, especially in the region of vibrational nodes.

Figure 3-8 shows similar reconstructions for the (2, 2) mode, which occurs at 1540 Hz. In the top row, the magnitude matches approximately the maximum object motion. The second row shows the results when the vibration magnitude of the reference-wave mirror is less than that of the object antinodes.

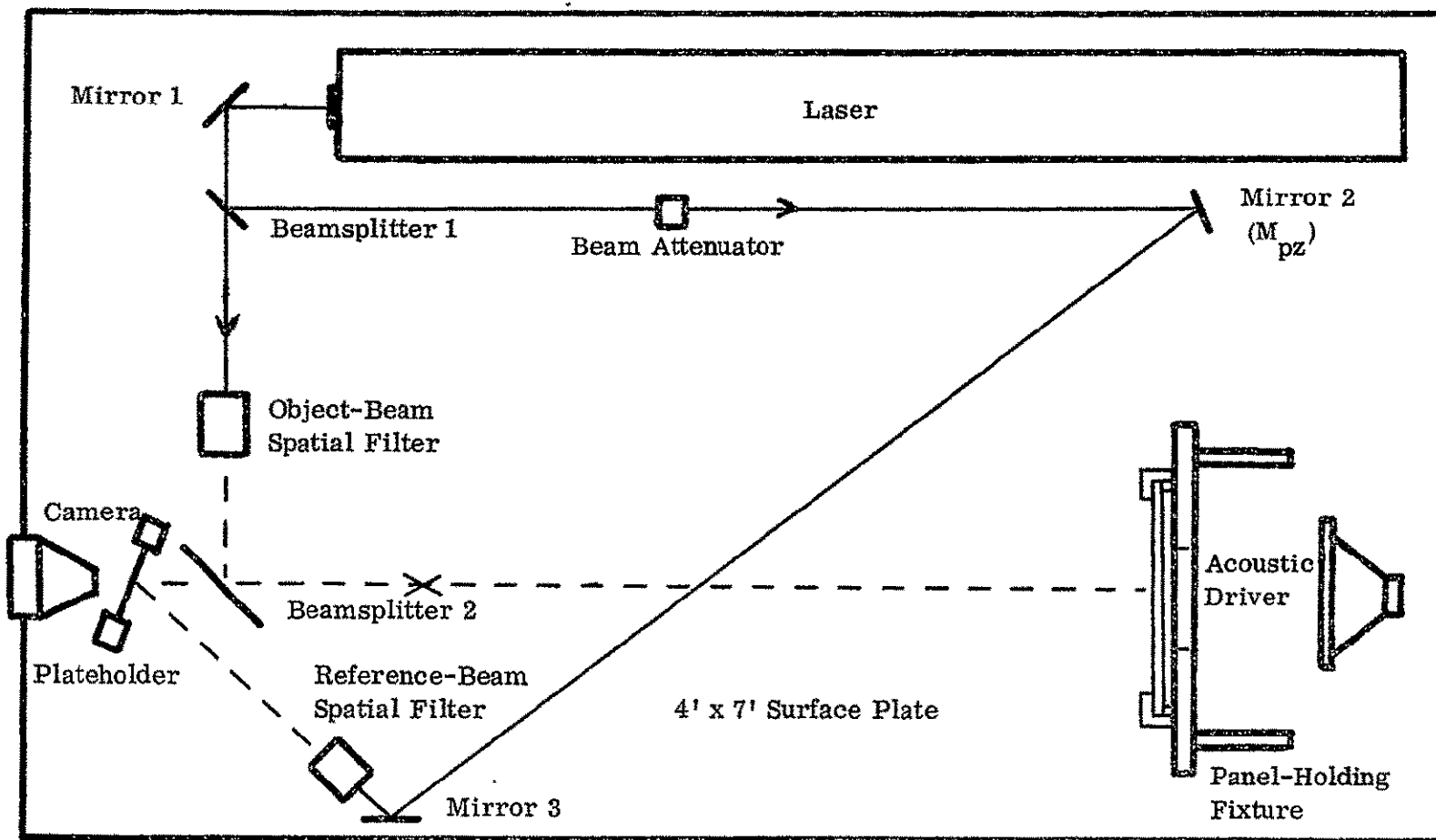
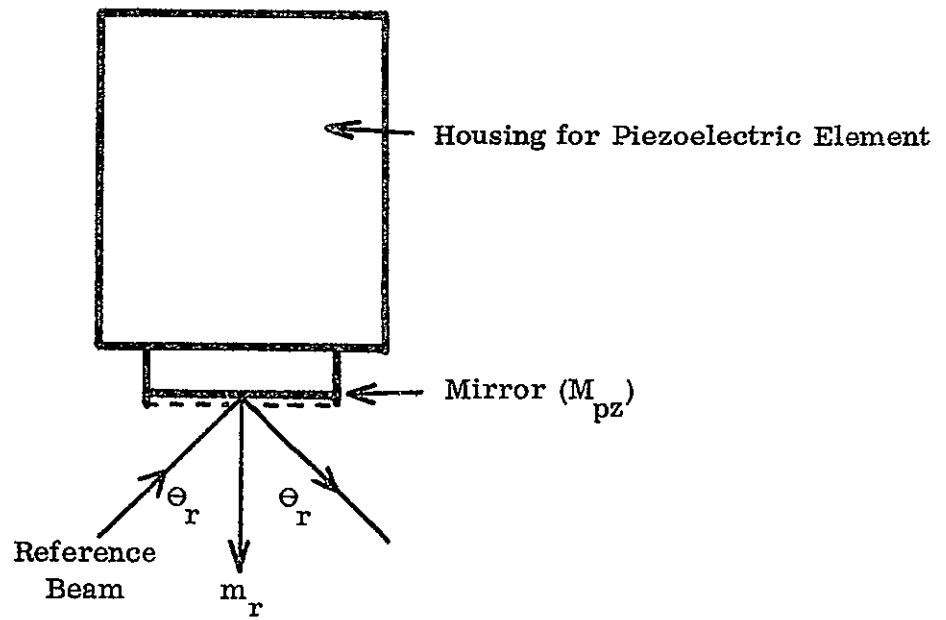


Fig. 3-5. Schematic Diagram of Holographic Interferometric System for Panel-Vibration Analysis with Phase-Shifted Reference Beam



$$\begin{aligned} \text{Phase Shift} &= k\Delta_r \sin \omega t \\ &= \frac{2\pi}{\lambda} m_r (2 \cos \theta_r) \sin \omega t , \end{aligned}$$

where  $m_r$  = Vibration amplitude

Fig. 3-6. Geometry of Vibrating Mirror,  $M_{pz}$ , in Reference Beam

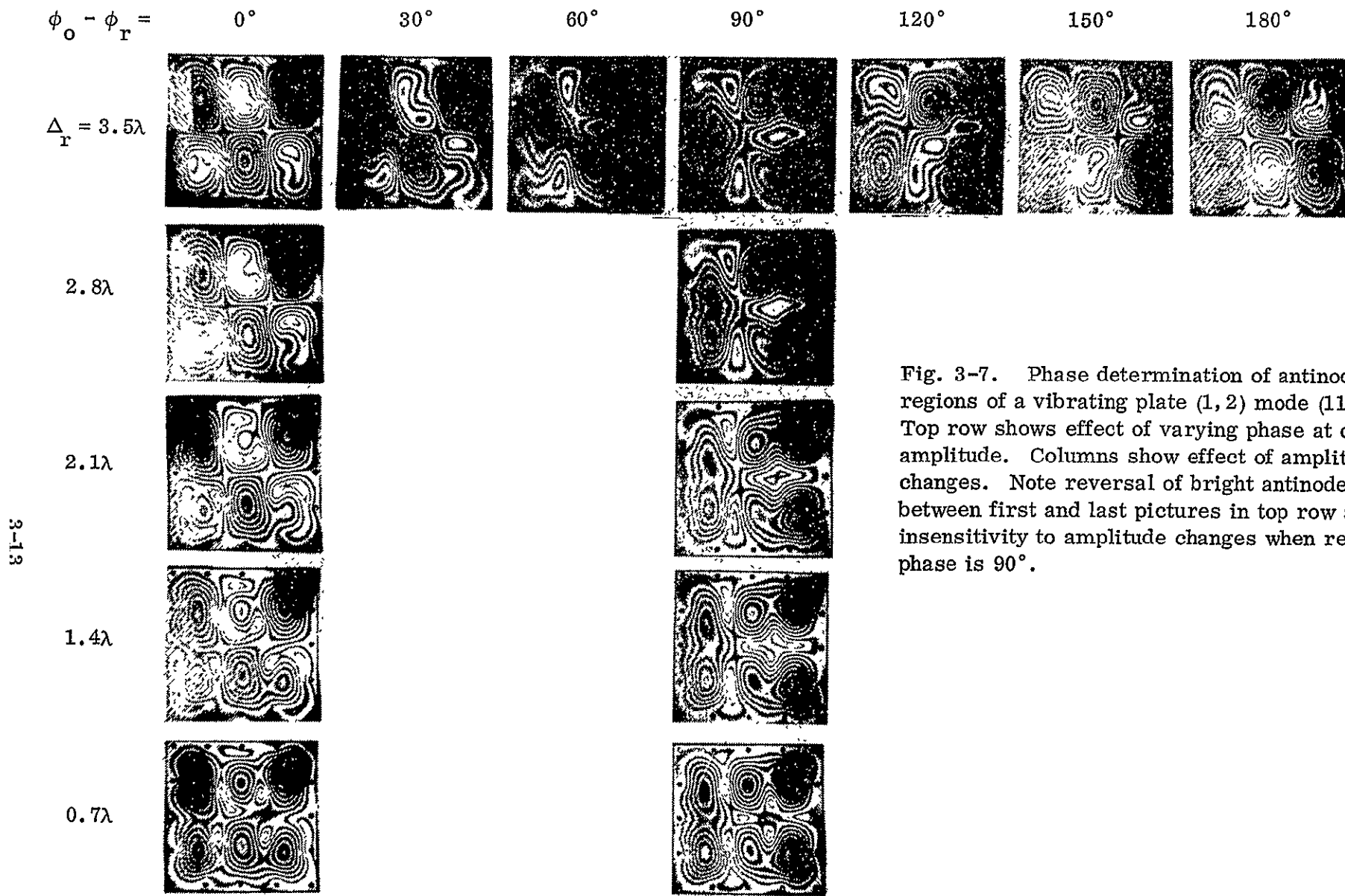
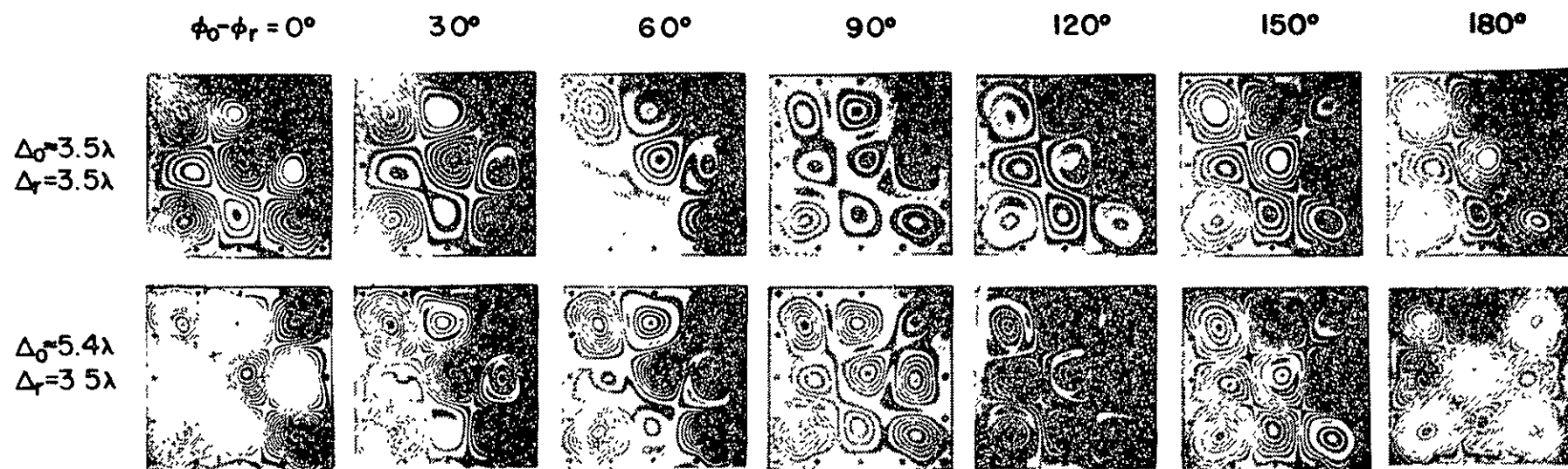


Fig. 3-7. Phase determination of antinodal regions of a vibrating plate (1, 2) mode (1165 Hz). Top row shows effect of varying phase at constant amplitude. Columns show effect of amplitude changes. Note reversal of bright antinodes between first and last pictures in top row and insensitivity to amplitude changes when relative phase is  $90^\circ$ .



NOT REPRODUCIBLE

Fig. 3-8. Phase determination for (2,2) mode (1540Hz) of a vibrating plate. Top row shows results when reference-wave shift is equal to antinode amplitude. Bottom row shows results when reference wave shift magnitude is less than object amplitude.

## 4.0 SHUTTERED-LASER PHASE MEASUREMENT

### 4.1 Theory

The shuttered argon laser system can be used for both "real-time" and "double-exposure" holographic interferometry. In the "real-time" case interference occurs between a reconstructed holographic image and the object wavefront and is observed (or photographed) in real time. In the "double-exposure" case interference occurs between two reconstructed images and must be observed at a later time.

Recall that in the real-time case the instantaneous intensity (I) of any point on the object observed through the holographic interferometer is given by:

$$I(t) = |E_o|^2 [a^2 + 1 + 2a \cos (\phi_\epsilon - k\Delta \sin \omega t)], \quad (4-1)$$

where

$E_o$  = object amplitude field

$a$  = constant

$\phi_\epsilon$  = phase difference caused by hologram-placement error or intentional object displacement

$k\Delta = 2\pi/\lambda (\cos \Theta_1 - \cos \Theta_2) m(x, y, z)$

$\lambda$  = laser wavelength

$m(x, y, z)$  = peak vibration amplitude at point (x, y, z) on the object

$\Theta_1$  = angle between vibration vector at object point (x, y, z) and the propagation vector of the incident laser-light illumination beam

$\Theta_2$  = angle between propagation vector of the laser light scattered from an object point (x, y, z) through the holographic plate to the point of observation.

We observe in real time while strobing with a pulse length,  $\Delta t$ , timed to pulse symmetrically at either the maximum or minimum of  $\sin \omega t$ . In other words:

$$I(t) = |E_o|^2 [a^2 + 1 + 2a \cos (\phi_\epsilon - k\Delta \sin \omega t)]$$

for

$$\left( \frac{\pi}{2} - \frac{\omega \Delta t}{2} \right) \leq \omega t \leq \left( \frac{\pi}{2} + \frac{\omega \Delta t}{2} \right)$$

$I(t) = 0$  for all other  $\omega t$ .

For small  $\Delta t$  and  $\omega t = (2n + 1) \pi/2$ :

$$\langle 1 \rangle = \left( \frac{\omega}{2\pi} \Delta t \right) |E_0|^2 [1 + a^2 + 2a \cos(\phi_\epsilon \pm k\Delta)] \quad (4-2)$$

[The term,  $(\frac{\omega}{2\pi} \Delta t)$ , represents the shuttering duty cycle.] The fringes can be given good visibility by adjusting  $(a)$  to near unity. The influence of  $\phi_\epsilon$  can be obtained by photographing the real-time static fringe system.

For larger  $\Delta t$ , rewrite the cosine term in Eq. (4-1):

$$\begin{aligned} g(t) &= \cos(\phi_\epsilon - k\Delta \sin \omega t) \\ &= \cos \phi_\epsilon \cos k\Delta \sin \omega t + \sin \phi_\epsilon \sin k\Delta \sin \omega t \\ &= \cos \phi_\epsilon [J_0(k\Delta) + 2 \sum_{n=1}^{\infty} J_{2n}(k\Delta) \cos(2n\omega t)] \\ &\quad + \sin \phi_\epsilon [2 \sum_{n=0}^{\infty} J_{2n+1}(k\Delta) \sin(2n+1)\omega t] \end{aligned} \quad (4-3)$$

Take the time-average of Eq. (4-3):

$$\begin{aligned} \langle g(t) \rangle &= \frac{\omega}{2\pi} \int_{\pi/2\omega - \Delta t/2}^{\pi/2\omega + \Delta t/2} g(t) dt \\ &= \frac{\omega \cos \phi_\epsilon}{2\pi} [J_0(k\Delta) t + 2 \sum_{n=1}^{\infty} J_{2n}(k\Delta) \frac{\sin 2n\omega t}{2n\omega}] \\ &\quad + \frac{\omega \sin \phi_\epsilon}{2\pi} [2 \sum_{n=0}^{\infty} J_{2n+1}(k\Delta) \frac{\cos(2n+1)\omega t}{(2n+1)\omega}] \Bigg|_{\pi/2\omega - \Delta t/2}^{\pi/2\omega + \Delta t/2} \end{aligned} \quad (4-4)$$

By changing the limits of integration, we can rewrite this equation as:

$$\begin{aligned} \langle g(t) \rangle &= \frac{\omega \cos \phi_\epsilon}{2\pi} [J_0(k\Delta) t + 2 \sum_{n=1}^{\infty} J_{2n}(k\Delta) (-1)^n \frac{\cos 2n\omega t}{2n\omega}] \\ &\quad - \frac{\omega \sin \phi_\epsilon}{2\pi} [2 \sum_{n=0}^{\infty} J_{2n+1}(k\Delta) (-1)^n \frac{\sin(2n+1)\omega t}{(2n+1)\omega}] \Bigg|_{\Delta t/2}^{\Delta t/2} \end{aligned} \quad (4-5)$$

By inspection the even Bessel series is zero over this limit, and we have:

$$\langle g(t) \rangle = \frac{\omega}{2\pi} \cos \phi_\epsilon J_0(k\Delta) \Delta t - \frac{\sin \phi_\epsilon}{2} \left[ \frac{4}{\pi} \sum_{n=0}^{\infty} J_{2n+1}(k\Delta) (-1)^n \frac{\sin(2n+1)\omega \frac{\Delta t}{2}}{(2n+1)} \right] \quad (4-6)$$

Consider the special case where we strobe over a half cycle of vibration ( $\Delta t = \pi/\omega$ ) \* then:

$$\langle g(t) \rangle \Big|_{\Delta t = \pi/\omega} = \frac{\cos \phi_\epsilon}{2} J_0(k\Delta) - \frac{\sin \phi_\epsilon}{2} \left[ \frac{4}{\pi} \sum_{n=0}^{\infty} J_{2n+1}(k\Delta) \right]. \quad (4-7)$$

The term in the brackets is equal to the zero-order Struve function, \*\*  $[H_0(k\Delta)]$ , allowing us to rewrite the equation as:

$$\langle g(t) \rangle \Big|_{\Delta t = \pi/\omega} = \frac{\cos \phi_\epsilon}{2} J_0(k\Delta) - \frac{\sin \phi_\epsilon}{2} H_0(k\Delta) \quad (4-8)$$

Time averaging Eq. (4-1) and rewriting it to incorporate these results gives:

$$\langle I \rangle = \frac{|E_0|^2}{2} \{ 1 + a^2 + 2a [\cos \phi_\epsilon J_0(k\Delta) - \sin \phi_\epsilon H_0(k\Delta)] \} \quad (4-9)$$

If  $\phi_\epsilon$  is constant over the object and  $\phi_\epsilon = n\pi$  ( $n = 0, 1, 2, \dots$ ), then:

$$\langle I \rangle = \frac{|E_0|^2}{2} [1 + a^2 + 2a(-1)^n J_0(k\Delta)], \quad (4-10)$$

and the fringes occur at either the maxima or minima of  $J_0(k\Delta)$ . If  $\phi_\epsilon$  is constant over the object and  $\phi_\epsilon = (2n+1)\pi/2$  ( $n = 0, 1, 2, 3, \dots$ ), then:

$$\langle I \rangle = \frac{|E_0|^2}{2} [1 + a^2 - 2a(-1)^n \sin \phi_\epsilon H_0(k\Delta)]. \quad (4-11)$$

For large arguments, in our case  $k\Delta \gg 2$ , we can use the asymptotic expansion formulas. \*\*\* We are mainly concerned with the arguments at the maxima and minima of  $J_0$  and  $H_0$  and not with their magnitudes. For large arguments we can write the asymptotic expansion of  $J_0(k\Delta)$ :

$$J_0(k\Delta) = \left(\frac{\pi}{2k\Delta}\right)^{1/2} \cos\left(k\Delta - \frac{\pi}{4}\right). \quad (4-12)$$

It is also known that the asymptotic expansion of  $H_0(k\Delta)$  can be obtained from:

$$H_0(z) - Y_0(z) = \frac{2}{\pi} \left[ \frac{1}{z} - \frac{1}{z^3} + \frac{1^2 \cdot 3^2}{z^5} - \frac{1^2 \cdot 3^2 \cdot 5^2}{z^7} + \dots \right] ****, \quad (4-13)$$

\* We cannot actually strobe over a half cycle, as the driver for the Pockell's cell is limited to about 5-percent duty cycle.

\*\* Handbook of Mathematical Functions, NBS, AMS 55, Par. 12.1.19, p. 497.

\*\*\* Mathematical Methods for Scientists and Engineers, p. 353, Lloyd P. Smith, Prentice Hall (1953).

\*\*\*\* Handbook of Mathematical Functions, NBS, AMS 55, Par. 12.1.30, p. 497.



because for large  $z$  the series rapidly converges to zero, and  $H_0(z) \cong Y_0(z)$  (the significant difference is  $H_0(0) = 0$  and  $Y_0(0) = -\infty$ ). The asymptotic expansion of  $Y_0$  for large  $z$  is given by:

$$H_0(k\Delta) \approx Y_0(k\Delta) \approx \left(\frac{\pi}{2k\Delta}\right)^{1/2} \sin\left(k\Delta - \frac{\pi}{4}\right) . \quad (4-14)$$

Equation (4-9) becomes:

$$\begin{aligned} \langle I \rangle = & \frac{|E_0|^2}{2} \left\{ 1 + a^2 + 2a \left(\frac{\pi}{2k\Delta}\right)^{1/2} [\cos \phi_\epsilon \cos\left(k\Delta - \frac{\pi}{4}\right) \right. \\ & \left. - \sin \phi_\epsilon \sin\left(k\Delta - \frac{\pi}{4}\right)] \right\} , \end{aligned} \quad (4-15)$$

which may be simplified to:

$$\langle I \rangle \cong \frac{|E_0|^2}{2} \left\{ 1 + a^2 + 2a \left(\frac{\pi}{2k\Delta}\right)^{1/2} [\cos(\phi_\epsilon + k\Delta - \frac{\pi}{4})] \right\} . \quad (4-16)$$

The fringe system represented by this equation is directly analyzed. We take a picture of the static fringe system due to  $\phi_\epsilon$ , the residual or error real-time static fringe system. Then we photograph the real-time vibrational fringe system after we've adjusted the position of the strobe or shutter pulse to illuminate the holographic interferometer only during either the plus or minus half-cycle of vibration.

The main drawback to the 50-percent-duty-cycle approach is that the fringe contrast is identical to that of the real-time nonshuttered case.

#### 4.2 Pulse-Length Requirement, $\Delta t$ , for Worst Case

The worst case occurs when we wish to observe the strobed real-time fringes at zero displacement where the velocity is maximum and correspondingly the fringes are moving fastest. The instantaneous interferometric intensity distribution was given in Eq. (4-1) as:

$$I(t) = |E_0|^2 [a^2 + 1 + 2a \cos(\phi_\epsilon - k\Delta \sin \omega t)] .$$

Time average the cosine term  $[g(t)]$  over the light pulse where the light pulse is centered on  $t_0$ :

$$\langle g(t) \rangle = \frac{\omega}{2\pi} \int_{t_0 - \Delta t/2}^{t_0 + \Delta t/2} \cos(\phi_\epsilon - k\Delta \sin \omega t) dt . \quad (4-17)$$

Change the limits, and rewrite as:

$$\langle g(t) \rangle = \frac{\omega}{2\pi} \int_{-\Delta t/2}^{\Delta t/2} \cos[\phi_\epsilon - k\Delta \sin(\omega t_0 + \omega x)] dx$$

$$= \frac{\omega}{2\pi} \int_{-\Delta t/2}^{\Delta t/2} \cos [\phi_{\epsilon} - k\Delta (\sin \omega t_0 \cos \omega x + \cos \omega t_0 \sin \omega x)] dx, \quad (4-18)$$

using  $x$  as a dummy variable.

In the special case where  $\omega t_0 = 0$ , this equation reduces to:

$$\langle g(t) \rangle = \frac{\omega}{2\pi} \int_{-\Delta t/2}^{\Delta t/2} \cos [\phi_{\epsilon} - k\Delta \sin \omega x] dx \quad (4-19)$$

Assume that  $\Delta t$  is small enough so that we can use the small-angle approximation,  $\sin \omega x \rightarrow \omega x$ , and Eq. (4-14) becomes:

$$\begin{aligned} \langle g(t) \rangle &= \frac{\omega}{2\pi} \cos \phi_{\epsilon} \int_{-\Delta t/2}^{\Delta t/2} \cos [(k\Delta)\omega x] dx + \left(\frac{\omega}{2\pi}\right) \sin \phi_{\epsilon} \int_{-\Delta t/2}^{\Delta t/2} \sin [(k\Delta)\omega x] dx \\ &= 2 \left(\frac{\omega}{2\pi}\right) \cos \phi_{\epsilon} \frac{\sin [(k\Delta)\omega \frac{\Delta t}{2}]}{(k\Delta)\omega} \end{aligned} \quad (4-20)$$

Multiply and divide by  $\frac{\Delta t}{2}$  and:

$$\langle g(t) \rangle = \frac{\omega \Delta t}{2\pi} \cos \phi_{\epsilon} \left\{ \frac{\sin [(k\Delta)\omega \frac{\Delta t}{2}]}{(k\Delta)\omega \frac{\Delta t}{2}} \right\} \quad (4-21)$$

The term in the brackets is the sinc function, whose value is unity for  $\Delta t \rightarrow 0$ . If the argument  $(k\Delta)\omega \Delta t/2$  is less than  $\pi/2$  at the  $\Delta_{\max}$  position on the object, then:

$$\frac{\sin (k\Delta)\omega \frac{\Delta t}{2}}{(k\Delta)\omega \frac{\Delta t}{2}} > \frac{2}{\pi} = 0.64 \quad (4-22)$$

Let this inequality be the criterion for determining either the allowable duty cycle ( $f\Delta t$ ) for a given amplitude ( $m/\lambda$ ) or the allowable amplitude for a given duty cycle. If the ideal visibility of static fringes is unity, then the fringe visibility under this criterion would not be less than  $2/\pi$  (0.64). Mathematically then:

$$(k\Delta)\omega \frac{\Delta t}{2} = \frac{2\pi}{\lambda} (2m) \frac{\omega \Delta t}{2} \leq \frac{\pi}{2} \quad (4-23)$$

$$\frac{m}{\lambda} \leq \frac{1}{8\pi f \Delta t}, \quad (4-24)$$

where  $f$  = frequency of vibration.

#### 4.3 Pulse-Length Requirement, $\Delta t$ , for Best Case

We have noted that for  $\omega t_0 = \pi/2$  and for small  $\omega \Delta t$  the characteristic function describing the fringeing is of the form:

$$1 + \cos (k\Delta + \phi_\epsilon).$$

For  $\Delta t = \pi$  the characteristic function is of the form:

$$1 + \cos \phi_\epsilon J_0(k\Delta),$$

which results in poor fringe visibility.

Let us now consider the intermediate case, where  $0 < \omega \Delta t < \pi$ :

$$\begin{aligned} \langle g(t) \rangle &= \frac{\omega}{2\pi} \int_{t_0 - \Delta t/2}^{t_0 + \Delta t/2} \cos (\phi_\epsilon + k\Delta \sin \omega t) dt \\ &= \int_{-\Delta t/2}^{\Delta t/2} \cos [\phi_\epsilon + k\Delta \sin (\omega t_0 + \omega t)] dt \\ &= \frac{\omega}{2\pi} \int_{-\Delta t/2}^{\Delta t/2} \cos [\phi_\epsilon + k\Delta (\sin \omega t_0 \cos \omega t + \cos \omega t_0 \sin \omega t)] dt. \end{aligned} \quad (4-25)$$

At  $\omega t_0 = \frac{\pi}{2}$ ,

$$\langle g(t) \rangle = \frac{\omega}{2\pi} \int_{-\Delta t/2}^{\Delta t/2} \cos [\phi_\epsilon + k\Delta \cos \omega t] dt \quad (4-26)$$

Approximate by expanding  $\cos \omega t$  in a Taylor series:

$$\begin{aligned} \langle g(t) \rangle &= \frac{\omega}{2\pi} \int_{-\Delta t/2}^{\Delta t/2} \cos \left( \phi_\epsilon + k\Delta - k\Delta \frac{\omega^2 t^2}{2} \right) dt \\ &= \frac{\omega}{2\pi} \cos (\phi_\epsilon + k\Delta) \int_{-\Delta t/2}^{\Delta t/2} \cos k\Delta \frac{(\omega t)^2}{2} dt \\ &\quad + \frac{\omega}{2\pi} \sin (\phi_\epsilon + k\Delta) \int_{-\Delta t/2}^{\Delta t/2} \sin k\Delta \frac{(\omega t)^2}{2} dt \\ &= \frac{\omega}{\pi} \cos (\phi_\epsilon + k\Delta) \int_0^{\Delta t/2} \cos k\Delta \frac{\omega^2 t^2}{2} dt \\ &\quad + \frac{\omega}{\pi} \sin (\phi_\epsilon + k\Delta) \int_0^{\Delta t/2} \sin k\Delta \frac{\omega^2 t^2}{2} dt \end{aligned} \quad (4-27)$$

If  $k\Delta$  is non-zero, that is, there is vibration, let

$$\frac{\pi}{2} \sigma^2 = \frac{(k\Delta)\omega^2 t^2}{2} ;$$

then

$$\sigma = \sqrt{\frac{2}{\pi}} \sqrt{\frac{(k\Delta)\omega^2}{2}} t = \sqrt{\frac{(k\Delta)\omega^2}{\pi}} t ;$$

$$dt = \sqrt{\frac{\pi}{(k\Delta)\omega^2}} d\sigma ;$$

and let

$$\xi = \sqrt{\frac{(k\Delta)\omega^2}{\pi}} \cdot \frac{\Delta t}{2} .$$

Then  $\langle g(t) \rangle$  (Eq. 4-27) reduces to:

$$\begin{aligned} \langle g(t) \rangle &= \frac{\omega}{\pi} \cos(\phi_\epsilon + k\Delta) \left[ \frac{\pi}{(k\Delta)\omega^2} \right]^{1/2} \int_0^\xi \cos \frac{\pi}{2} \sigma^2 d\sigma \\ &+ \frac{\omega}{\pi} \sin(\phi_\epsilon + k\Delta) \left[ \frac{\pi}{(k\Delta)\omega^2} \right]^{1/2} \int_0^\xi \sin \frac{\pi}{2} \sigma^2 d\sigma \\ &= \frac{\omega}{\pi} \left[ \frac{\pi}{(k\Delta)\omega^2} \right]^{1/2} [\cos(\phi_\epsilon + k\Delta) C(\xi) + \sin(\phi_\epsilon + k\Delta) S(\xi)], \quad (4-28) \end{aligned}$$

where  $C(\xi)$  and  $S(\xi)$  are Fresnel integrals.

Noting that  $\left[ \frac{\pi}{(k\Delta)\omega^2} \right]^{1/2} = \frac{\Delta t}{2\xi}$  and factoring out  $[C^2(\xi) + S^2(\xi)]^{1/2}$ , rewrite Eq. (4-28) as:

$$\langle g(t) \rangle = \frac{\omega \Delta t}{\pi 2} \left[ \frac{C^2(\xi) + S^2(\xi)}{\xi^2} \right]^{1/2} \frac{\cos(\phi_\epsilon + k\Delta) C(\xi) + \sin(\phi_\epsilon + k\Delta) S(\xi)}{[C^2(\xi) + S^2(\xi)]^{1/2}} \quad (4-29)$$

Let:

$$\frac{C(\xi)}{[C^2(\xi) + S^2(\xi)]^{1/2}} = \cos(\psi),$$

$$\frac{S(\xi)}{[C^2(\xi) + S^2(\xi)]^{1/2}} = \sin(\psi),$$

and

$$\psi = \tan^{-1} \left[ \frac{S(\xi)}{C(\xi)} \right]$$

Then:

$$\langle g(t) \rangle = \frac{\omega \Delta t}{2} \left[ \frac{C^2(\xi) + S^2(\xi)}{\xi^2} \right]^{1/2} \cos(\phi_\epsilon + k\Delta - \psi) \quad (4-30)$$

The term  $\psi$  is of only minor importance:

$$(0 < \psi < \frac{\pi}{4}) .$$

Of major interest is the magnitude of the term in the square-root bracket. It weights the observed fringe system from the ideal case (characteristic function =  $1 + \cos(\phi_\epsilon + k\Delta)$ ). We therefore look at:

$$[Q(\xi)]^{1/2} = \left[ \frac{C^2(\xi) + S^2(\xi)}{\xi^2} \right]^{1/2} \quad (4-31)$$

In the limit:

$$Q(\xi) \Big|_{\xi \rightarrow 0} = 1 .$$

From Fresnel integral tables we compute  $Q(\xi)$  for various values of  $\xi$ :

$\xi$	$Q(\xi)$	$[Q(\xi)]^{1/2}$
0	1	1.
0.2	0.99963	0.999
0.4	0.99439	0.997
0.6	0.97190	0.991
0.8	0.91354	0.956
1.0	0.80029	0.894
1.2	0.62535	0.790
1.4	0.41023	0.641
1.5	0.30433	0.552
1.54	0.26514	0.515
1.56	0.24653	0.5
		(0.4965)

We take the criterion that we want:

$$[Q(\xi)]^{1/2} > 0.5$$

Therefore:

$$\begin{aligned} \xi &\leq 1.56 \approx \frac{\pi}{2} \\ \xi &= \left( \frac{k\Delta}{\pi} \right)^{1/2} \cdot \frac{\omega \Delta t}{2} \leq \frac{\pi}{2} \end{aligned} \quad (4-32)$$

We wish to obtain  $m/\lambda$  in terms of  $f\Delta t$ :

$$\frac{m}{\lambda} \leq \frac{1}{16(f\Delta t)^2} \quad (4-33)$$

This equation is plotted in Fig. 4-1.

#### 4.4 Experiment Verification of Shuttered-Laser Phase Measurement

Phases of vibration of the antinodes on several vibrating plates were measured holographically by use of the shuttered-laser approach. The system schematic drawing is shown in Fig. 4-2. The peak displacement at each antinode was maximized by using the phase-shift control on the oscillator.

The results of these tests on a square panel and a circular panel are shown in Figs. 4-3, 4-4, 4-5, and 4-6. The peak displacements on the square panel are either in phase or  $180^\circ$  out of phase. The circular panel exhibited different phase shifts and so warranted closer examination.

In Fig. 4-5 (photos of real-time hologram reconstructions of a circular plate vibrating at 670 Hz in a (1, 1) mode), the measured phase difference between the two antinode peaks is  $205^\circ$  (instead of  $180^\circ$ ). This same plate had a second (1, 1) mode at 700 Hz, as shown in Fig. 4-6, with two antinodes vibrating  $20^\circ$  out of phase with each other.

Figures 4-5 and 4-6 are photographs of the plate with no vibration. The four static fringes were obtained by very slightly tilting the top of the plate-holding fixture back away from the observer. Before the tilting, two or three circular fringes were roughly centered on the disc. The tilt shifted the fringes down and somewhat to the left.

These static fringes can be used to resolve the  $180^\circ$  phase ambiguity that occurs with more than one antinode. Note in Fig. 4-5 the fringe that arches over from 10 o'clock to 4 o'clock. In (a) and (b) this fringe is not too greatly changed, but it is pushed down by the top-right antinode, indicating that this antinode is now closer to the observer, i. e., in the direction of its position before tilting.

Similar observations can be made about Fig. 4-6.

We believe that the existence of a (1, 1) mode at two distinct frequencies is due to anisotropic physical properties of the aluminum plate induced during the rolling processes.

The phenomenon of adjacent antinodes not being  $180^\circ$  out of phase may be due to a nonlinear effect. Figures 4-5(f) and 4-6(f), time-average reconstructions of these two modes, show more clearly the absence of a node between the two antinodes and indicate the presence of a fundamental component.

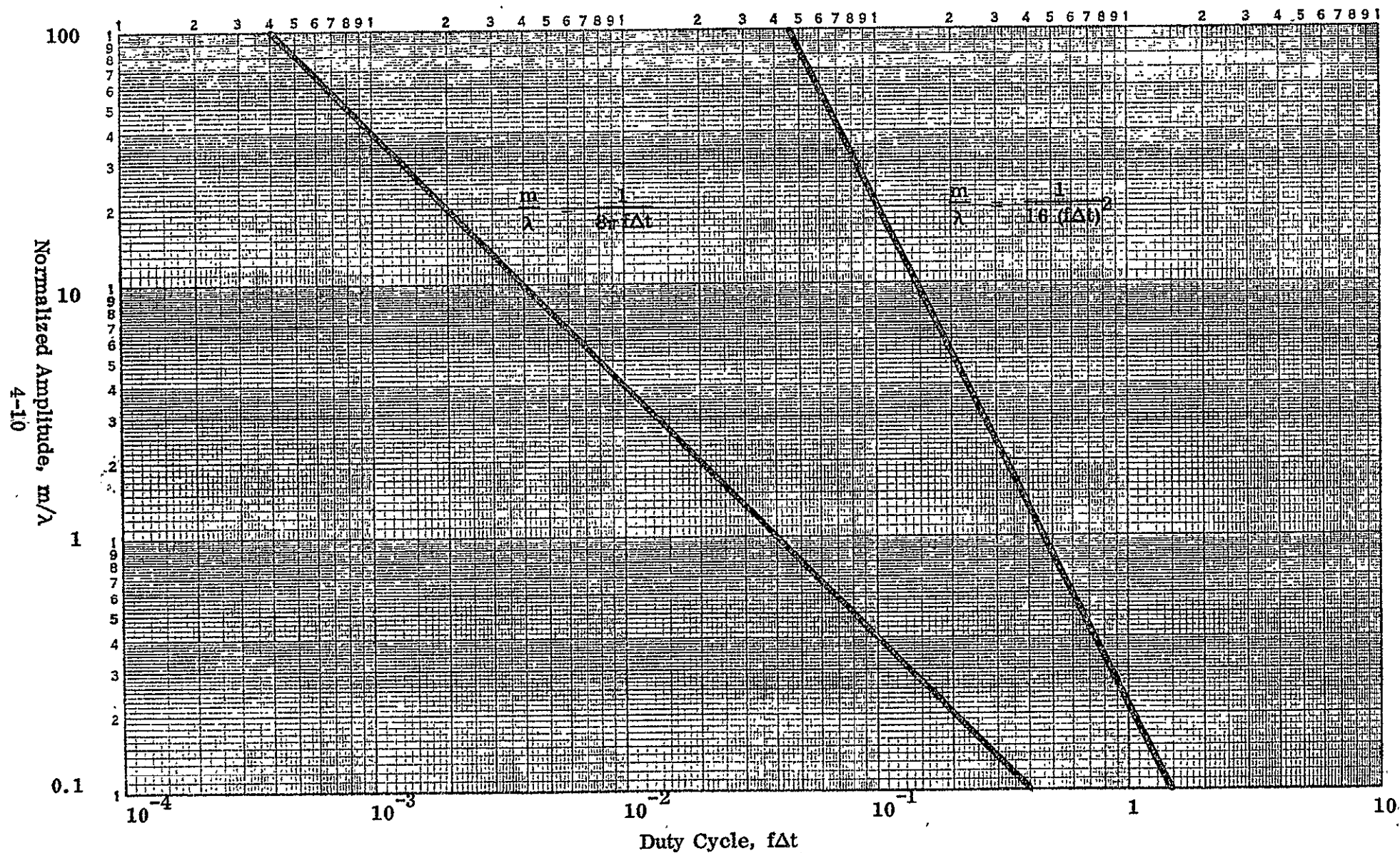


Fig. 4-1. Maximum Permissible Vibration-Amplitude versus Light-Pulse Duty Cycle to Accurately Freeze Real-Time Fringes in Strobbed-Laser Holography

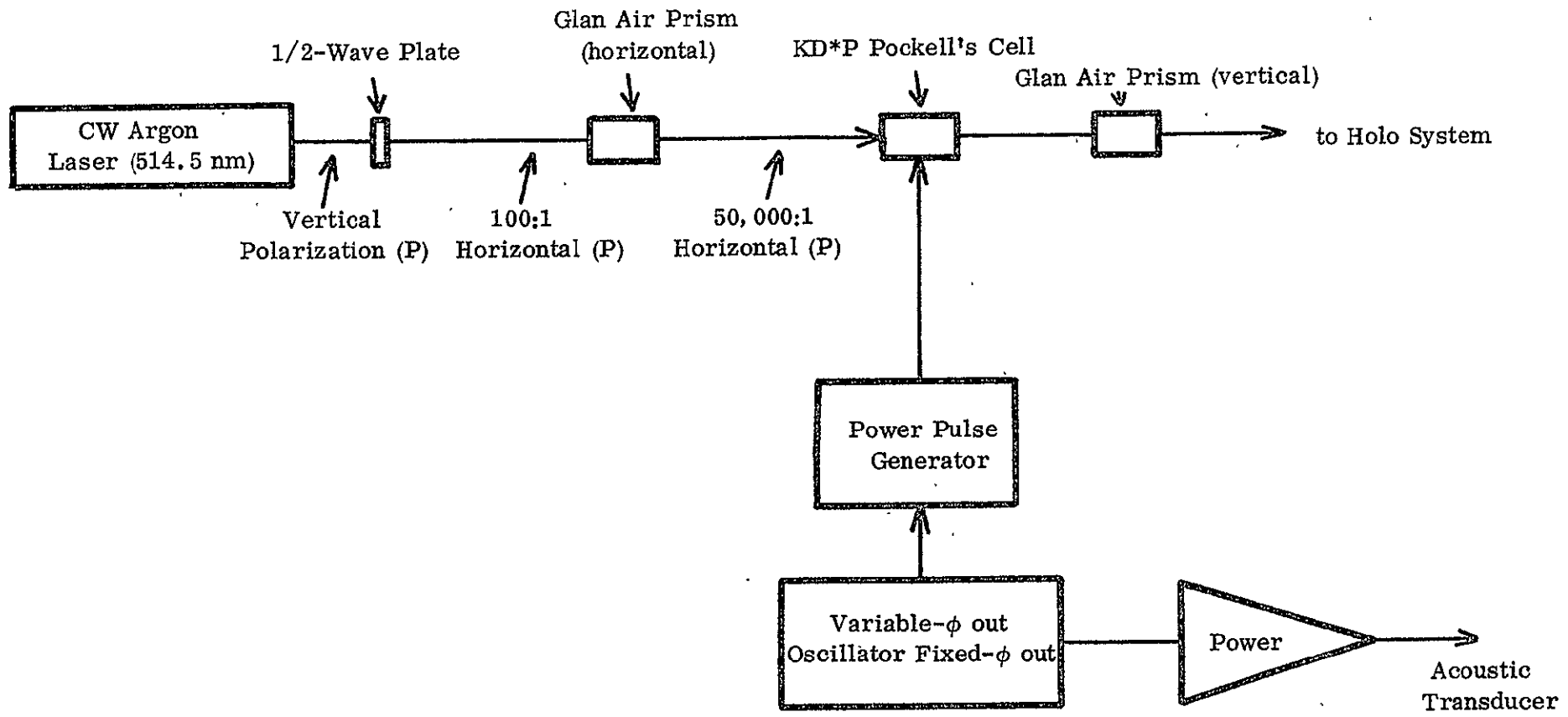
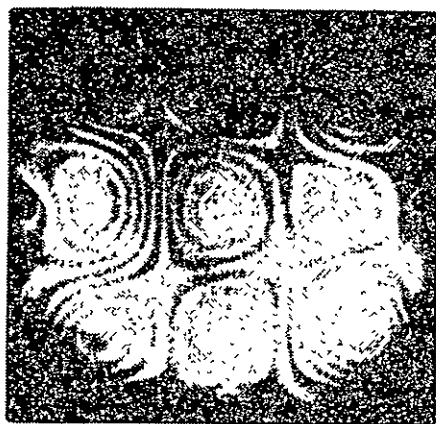
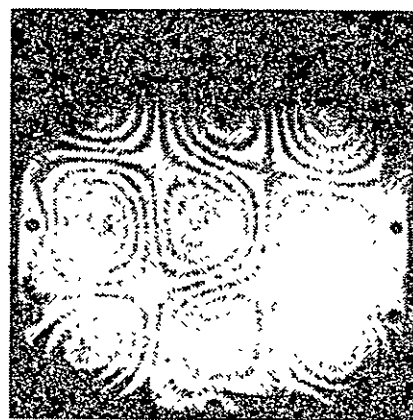


Fig. 4-2. Laser Shuttering System

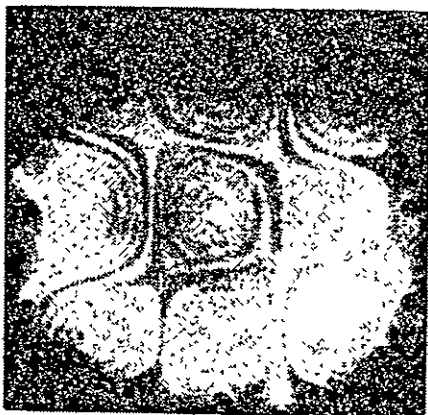




$\omega t_0 = 270^\circ$

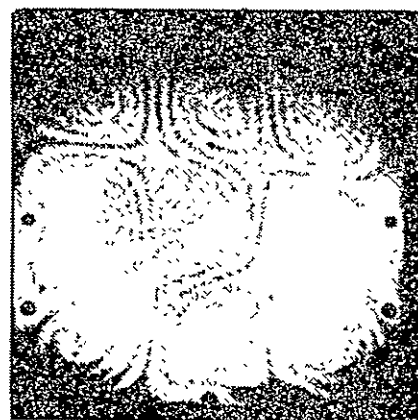


$\omega t = 90^\circ$



$240^\circ$

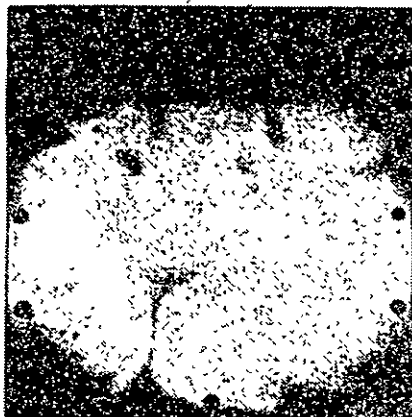
NOT REPRODUCIBLE



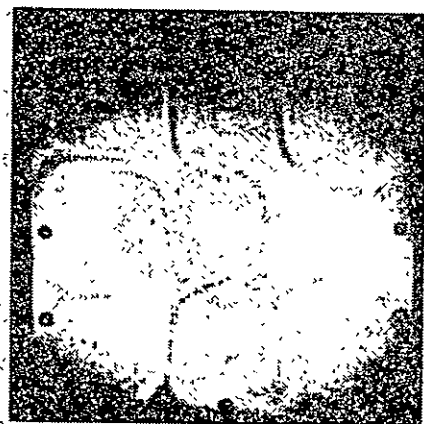
$120^\circ$



$210^\circ$

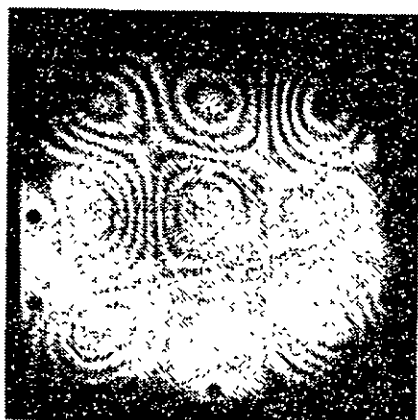


$180^\circ$

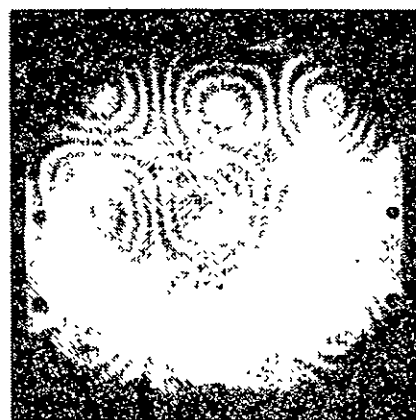


$150^\circ$

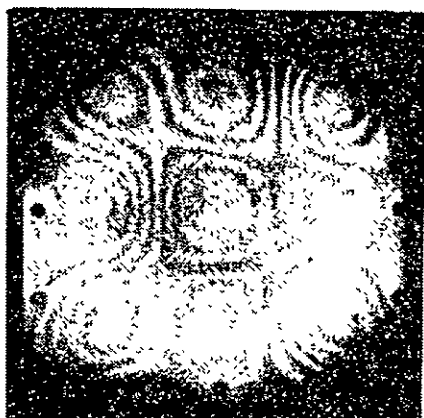
Fig. 4-3. Strobed real-time holographic interferometric fringes of a vibrating aluminum panel. Strobe time ( $\Delta t$ ) was  $100 \mu \text{ sec}$ , and the vibrational frequency was  $1300 \text{ Hz}$ .



$\omega t_0 = 270^\circ$

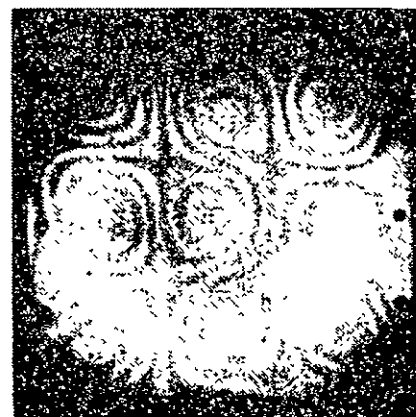


$\omega t = 90^\circ$

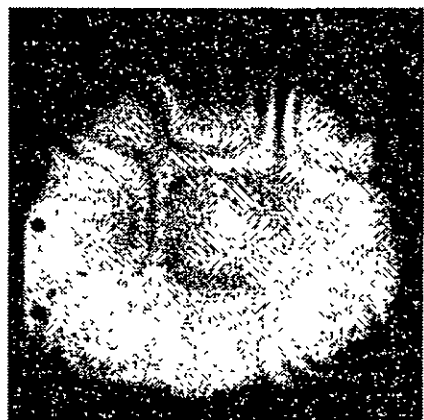


$240^\circ$

NOT REPRODUCIBLE



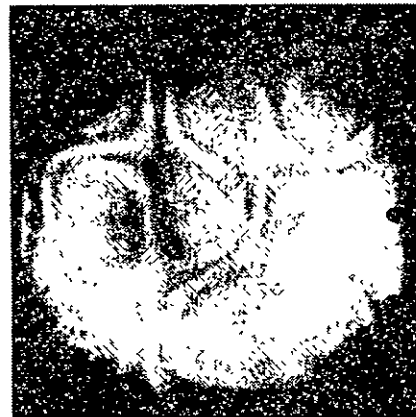
$120^\circ$



$210^\circ$



$180^\circ$



$150^\circ$

Fig. 4-4. Strobed real-time holographic interferometric fringes of a vibrating aluminum panel. Strobe time ( $\Delta t$ ) was  $30 \mu \text{ sec}$ , and the vibrational frequency was  $1300 \text{ Hz}$ .

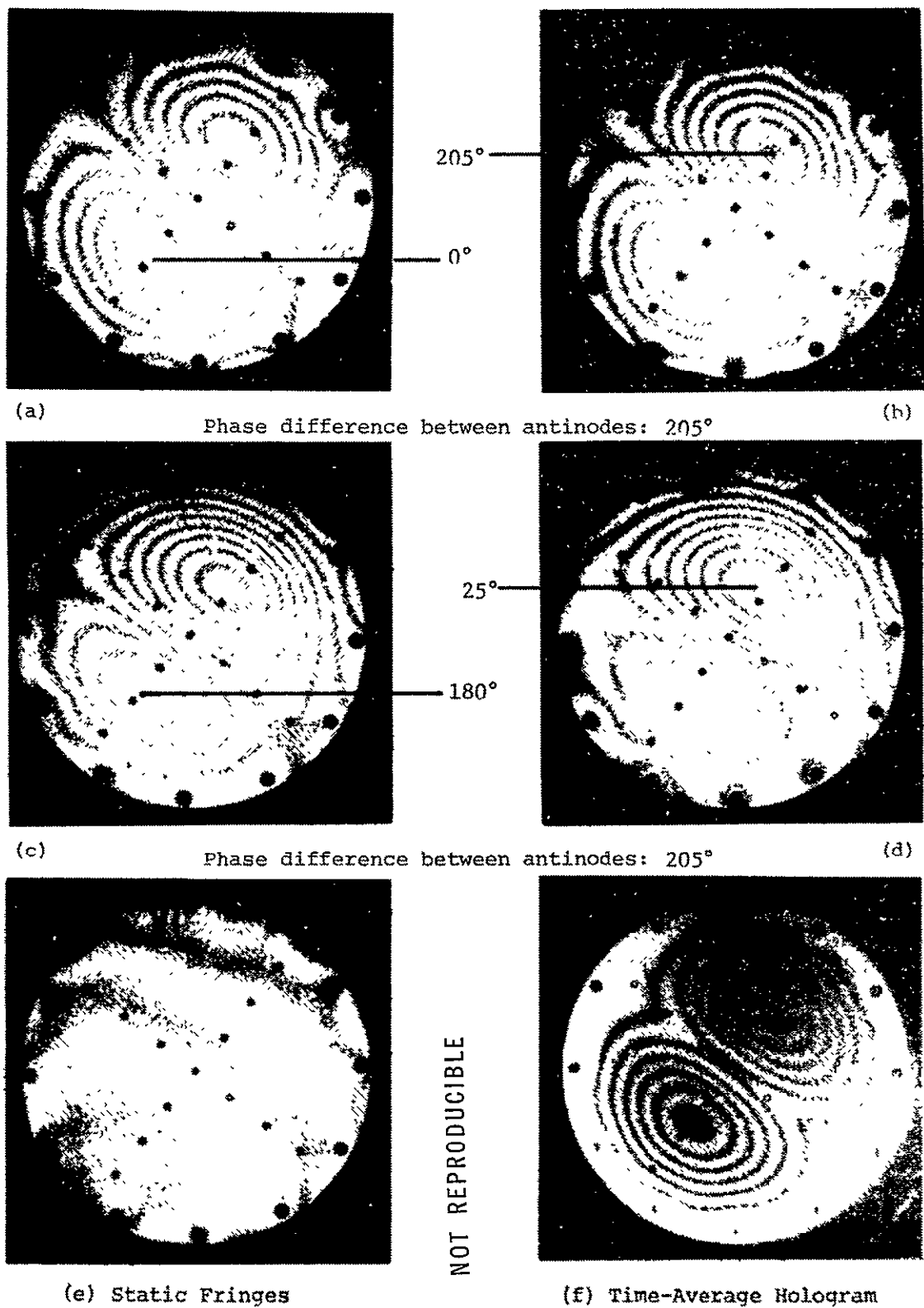


Fig. 4-5. Real-time holographic interferometric phase measurement of a circular plate vibrating in (1,1) mode at 670 Hz. Phase measured at antinode peaks.

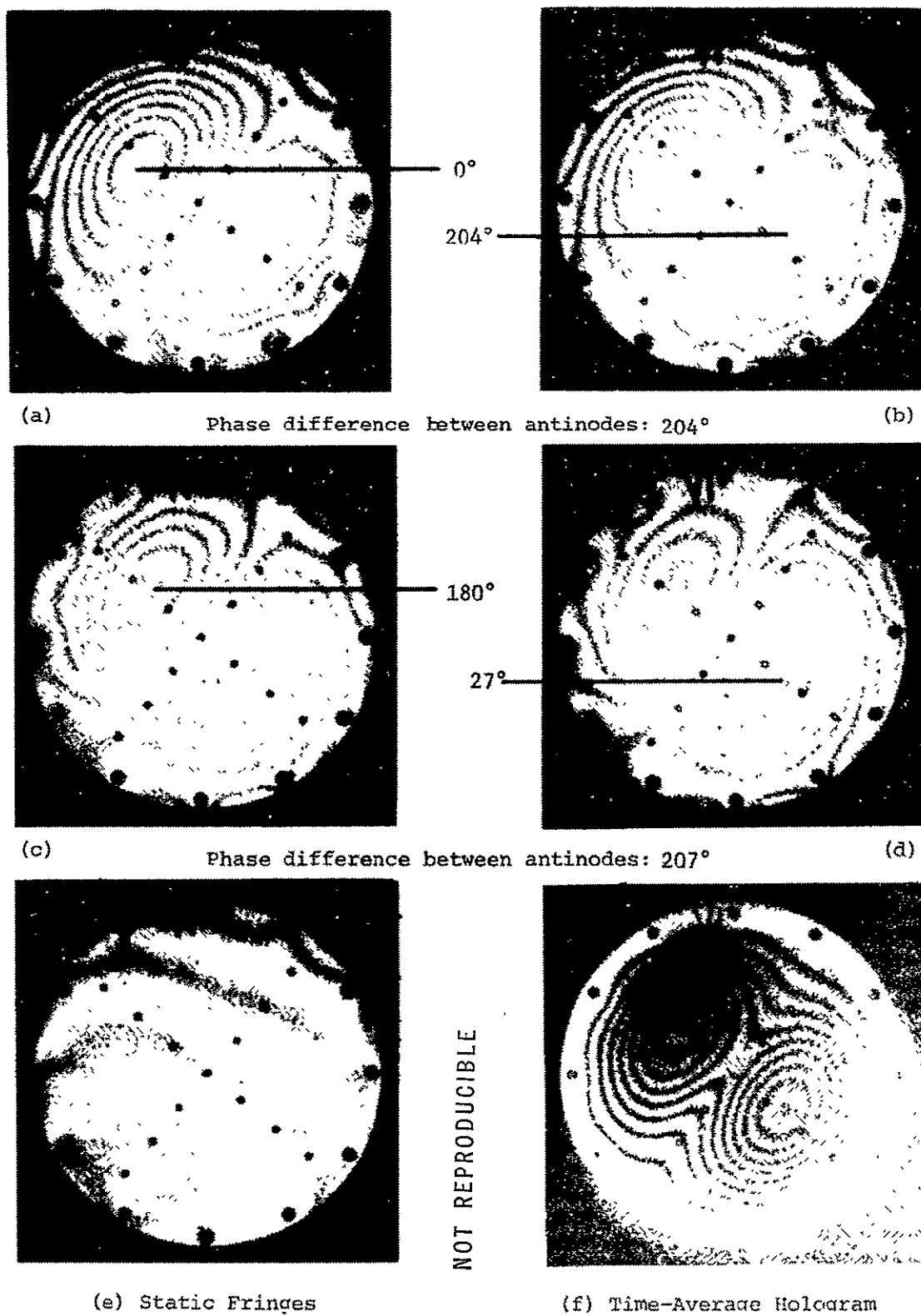


Fig. 4-6. Real-time holographic interferometric phase measurement of the same circular plate vibrating in another (1, 1) mode at 700 Hz. Phase measured at antinode peaks.

#### 4.5 Application Limitation

Generally, the real-time shuttered technique uses a hologram of the object recorded in static position, so interference at any instant occurs between static position and instantaneous dynamic position. In the time-average case discussed in section 2.5, the interference occurs between the two peak positions of the vibrating object. Because of this difference the limits and capabilities of real-time shuttered holographic interferometry are generally a factor of 2 different than for time-average holography. Specifically the results for both techniques are summarized in Table 4-I.

Table 4-I

#### Comparison of the Capabilities of Time-Average and Real-Time, Shuttered Holographic Interferometry (HI)

	<u>Holographic Interferometry</u>	
	<u>Time-Average</u>	<u>Real-Time Shuttered</u>
1. Displacement-Amplitude Accuracy Limit	a. 12.2 nm visual observation	a. 24.4 nm visual observation
2. Maximum-Amplitude Limit (max. change in slope of object)	488 nm/mm	976 nm/mm
Example for 20-inch panel vibrating	0.25 mm	0.5 mm
3. Minimum-Amplitude Limit	100 nm (visual)	a. 200 nm (visual) b. 1.0 nm (photo detect)
4. Vibration-Frequency Limitations	none	a. 500 kHz (strobe) b. 2 kHz (high-speed photography)
5. Measurable-Area Limitations		?

## 5.0 TRANSIENT ANALYSIS RESPONSE

To demonstrate the feasibility of using holographic techniques to study the transient response of an object, two systems were considered. An image-converter camera was studied because of its potential for light gain and its excellent fast shuttering capability necessary to photograph the expected high-frequency, fast-moving fringe systems caused by a shock input. An alternate consideration was to use the shuttered-laser system in conjunction with high-speed motion-picture photography.

### 5.1 Image-Converter Camera

A TRW image-converter camera, model ID3, was studied to determine its applicability for use in transient-phenomena and shock analysis in conjunction with real-time holographic interferometry. The main reasons for considering this device were its potential for light gain and its excellent fast-shuttering capability (as an alternative to the use of the shuttered argon laser).

From the manufacturer's literature it was determined that the required exposure to record an image would be approximately  $1.35 \times 10^{-12}$  watt-sec/cm<sup>2</sup> ( $13.5 \times 10^{-6}$  erg/cm<sup>2</sup>) at 514.5-nm wavelength, using the standard lens (125 mm, f/2) and 3000-speed Polaroid film.

This unit was evaluated at a near-by university laboratory. The image from a time-average hologram of a vibrating plate using a He-Ne laser (SP124) was reconstructed. This reconstructed image had a radiance of  $0.1 \times 10^{-6}$  watt/cm<sup>2</sup>. The minimum exposure time required to photograph the reconstruction with the image-converter camera was  $7 \times 10^{-3}$  sec. The exposure input to the camera, then, was  $7 \times 10^{-10}$  watt-sec/cm<sup>2</sup> ( $70 \times 10^{-4}$  erg/cm<sup>2</sup>) at 632.8-nm wavelength. At 514.5-nm wavelength the exposure input would be about half that value or  $3.5 \times 10^{-10}$  watt-sec/cm<sup>2</sup> ( $35 \times 10^{-4}$  erg/cm<sup>2</sup>).

Using the real-time holographic interferometric system with the argon laser (CRL 52) at full power, an object-interferometric radiance of about  $20 \times 10^{-6}$  watt/cm<sup>2</sup>, which would require an exposure time of  $1.8 \times 10^{-5}$  sec., was measured. The photographs (reproduced in actual size in Fig. 5-1) were obtained at exposures of  $6.7 \times 10^{-3}$ ,  $10^{-2}$ , and  $2 \times 10^{-2}$  sec.

It was concluded that this image-converter camera would achieve the same results as had already been achieved with the shuttered-CW laser but with some added complexity, some loss of resolution, and at greatly increased cost.

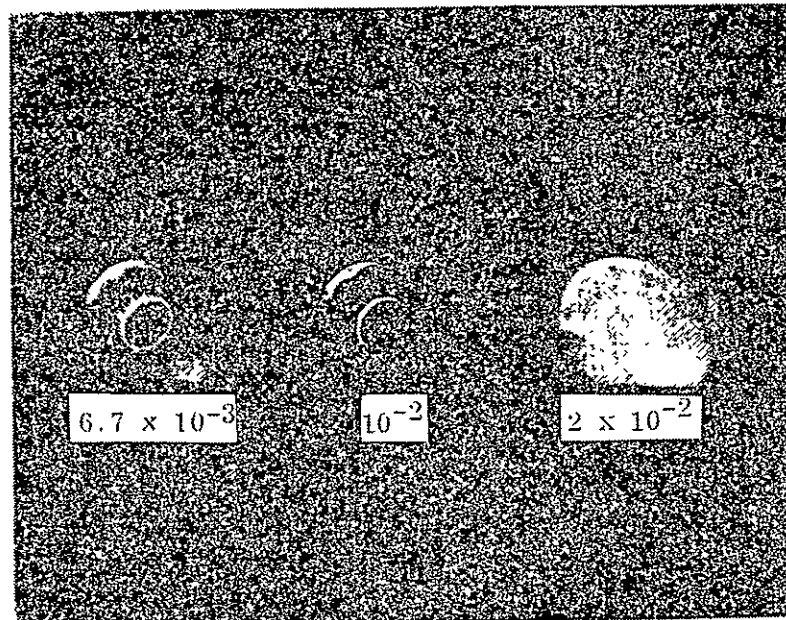


Fig. 5-1. Exposure time, seconds, for photographs by image-converter camera of reconstructed image of a vibrating plate

## 5.2 High-Speed Camera

NOT REPRODUCIBLE

The alternate method of using the shuttered-laser system was considered, but the timing and speed with which the photographs must be taken led to the consideration and application of high-speed photography of a real-time fringe system.

### 5.2.1 Shock Impulse (NASA Cylinder)

Real-time holographic fringes, occurring after a shock impulse on the 18-inch-diameter NASA cylinder, were photographed with a 16-mm, high-speed, Hycam camera made by Red Lake Labs. The filming rate was 5000 frames/sec. on Kodak 2484 black-and-white negative film. The impulse was initiated with a simple pendulum set to strike the side of the cylinder once. The pendulum was released by a signal from the camera after 25 feet of film had passed through. A 1/10 shutter in the camera gave an exposure time of 20 sec. for each frame. Although an argon laser was used for the filming, the light level was so low that the image was dim. To increase the image brightness several hologram-bleaching techniques were evaluated. The best results were obtained from Kodak Chrome Intensifier with Agfa 10E70 film in a fluid-gate plateholder.

The first 20 frames after the shock impulse showed the initial distortion of the cylinder. Figure 5-2 shows a sequence of 20 frames starting one frame before shock. The unintentional and undesirable fringe system present before shock

(frame 1) was caused by the object's holographically noticeable contraction and expansion with very small temperature changes. For example, the fringe structure on this object changed considerably even when the laboratory door was opened. The laboratory temperature was not closely controlled, as it was usually not necessary. Closer temperature control, along with environmental isolation of the holographic system from the operator and heat-generating instruments, would solve this problem.

### 5.2.2 Analysis of 7-inch Disks

To simplify the analysis of the transient response of a mechanical shock event, high-speed photography was repeated on a circular plate instead of the cylinder as the object. The objectives were also expanded to include the study of the transient response (1) to the removal of a steady-state forcing function at an object resonance and (2) to a step input, as well as (3) to shock impulse.

The optical setup and experimental procedures used were identical to the previous tests on the cylinder. A bleached hologram was used in one test with the shock input to allow shorter exposure, but the availability of a more powerful laser (CRL 53 argon, with 2-watt power) made the lengthy bleaching process unnecessary.

The object was a 7-inch-diameter circular plate made from 0.040-inch aluminum sandwiched between two steel rings. The boundary conditions were those of a classical fixed edge. The plate was coated with 3M Scotchlite retro-reflective coating to enhance brightness. This coating was used with on-axis illumination and viewing so the obliquity angle was zero.

The inputs for each test were controlled by a function switch in the camera. The switch was activated after 25 feet of film had gone through the Hycam, 16-mm, high-speed camera. The filming rate was 5000 pps and a 1/10 shutter was used, giving an exposure time of 20  $\mu$  sec. on each frame of Kodak 2484 black-and-white negative film.

A test film was made to determine the correct exposure and development process and to record the effect of camera noise on the plate. The vibration caused by the camera was appreciable and was present during each test and no effective means of removal was found. The noise made it impossible to perform detailed analysis on the fringe systems as it was not of constant amplitude. The mode excited by the camera noise tended to increase in amplitude as time progressed and as such its effect could not be determined and subtracted from the overall response. The response trends observed in each of the films will be commented upon, but individual photos will not be included because they do not contain any useful data not already included in the work previously described.

1. Removal of Steady-State Forcing Function. The steady-state forcing function was provided by an acoustical driver set at a resonant frequency (484 Hz)



of the plate. The driver was disconnected by the camera's function switch. The film recorded the fringe pattern of the transient decay from a system resonance.

The transient response from resonance was as expected. After the forcing function was removed, the vibrational amplitude decayed and the vibration remained at the second harmonic until the effect of the camera noise became non-negligible. The observed pattern tended to rotate due to extraneous driving signals, probably from the camera. The time of drive disconnect was not indicated on the film, and as such could not be determined for measurement purposes.

2. Step-function Impulse. The step-function input was accomplished by the removal of the constant deflection of the center of the plate. A small bolt was glued to the back side of the plate, which was deformed with a small solenoid. The effect of camera noise was seen at the beginning of the film strip when the deflection was constant and no vibrational structure should be present. When the function switch disconnected the solenoid, the film showed the fringe pattern of the transient response of the disk. Again, it was impossible to determine when the step actually occurred.

The qualitative results were as predicted by theory, after the step; the transient response was in the form of a damped sinusoidal vibration. In this case, it was the fundamental mode. Since the camera noise was also predominantly of the fundamental mode, accurate analysis would require the camera to be placed in an anechoic box.

3. Shock Impulse. The shock input was provided by a small ball bearing on a string. When released, the ball struck the back surface of the plate. The resultant fringe pattern showed the transient response to this shock impulse. The initial deflection was too great for fringe resolution, so no information could be obtained about maximum deflection after impact. Several resonant modes slightly revealed at the outset decayed very quickly. At impact, the fringe pattern indicated a radial resonance mode. After the maximum deflection occurred, the radial mode was still evident but disappeared quickly. When the deflections became small enough to keep the fringe frequency low, the plate was seen vibrating in a combination of the first and second harmonics with some indication of the third harmonic. The second harmonic became dominant and the plate stayed in that mode until the camera noise once more became dominant.

#### 5.2.3 Data Reduction

The experimental data obtained with the high-speed movie camera will have to be analyzed on a frame-by-frame basis to obtain quantitative results for surface displacements as a function of time. The problem was investigated during the course of the contract but no preferred method for reducing the data was discovered.

Data taken during the experiments described above was not analyzed because the effects of camera noise could not be eliminated and the sampling rate was found to be much too low for adequate data reduction.

The need for high data rates can be appreciated if one considers the analysis of a sinusoidally vibrating object. Application of conventional sampling theory would indicate a sampling rate of something more than twice the vibrational frequency; however, such is not the case for holographic analysis. The reason for this is that the amplitude of vibration is not directly related to the observed fringe system but is related through a cosine function which is ambiguous by module  $2\pi$ . To sort out the ambiguities requires sampling what is, in essence, an FM spectrum and sampling rates many times the vibrating frequency may be required.

The sampling rate must be such that only a portion of a fringe has passed an observation point during a sampling interval. Using a conventional holographic system one finds the phase of the observed fringe system expressible as:

$$2k a \sin \omega t \quad (5-1)$$

where  $a$  is the vibrational amplitude and  $\omega$  is the radian frequency of the vibration. To require less than a half fringe to pass a point (ambiguous sampling rate) between observation times  $t_1$  and  $t_2$  one finds the inequality

$$2k a (\sin \omega t_2 - \sin \omega t_1) \leq \frac{\pi}{2} \quad (5-2)$$

must be satisfied for all times  $t_1$ . Expression (5-2) may be reduced to the form

$$4k a \cos \frac{\omega}{2} (t_1 + t_2) \sin \frac{\omega}{2} (t_1 - t_2) \leq \frac{\pi}{2} \quad (5-3)$$

Letting  $t_1 - t_2 = \tau$ , the sampling interval, and requiring that (5-3) be satisfied for all values of  $t_1$  reduces (5-3) to the form

$$4k a \sin \frac{\omega \tau}{2} \leq \frac{\pi}{2} \quad (5-4)$$

Letting  $\omega = \frac{2\pi}{T}$ , where  $T$  is the period of vibration, reduced (5-4) to the form

$$\sin \pi \frac{\tau}{T} \leq \frac{\lambda}{16 a} \quad (5-5)$$

which may be approximated by

$$\frac{\tau}{T} = \frac{\lambda}{16 \pi a} \quad (5-6)$$

for  $a$  greater than  $\lambda$ .

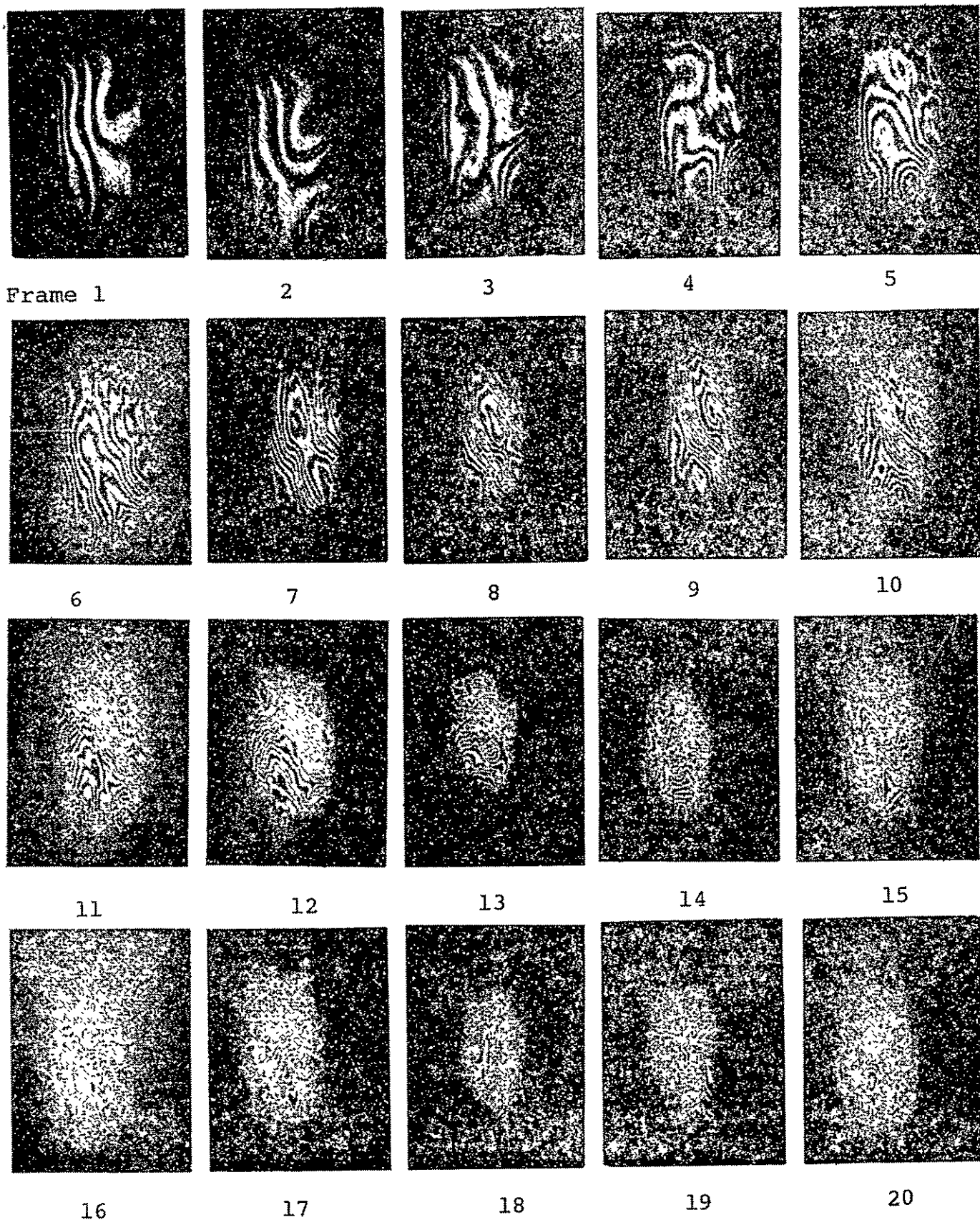


Fig. 5-2. Real-time holographic interferometric fringe system of 18-inch-diameter cylinder photographed by high-speed camera (5000 frames per second) after shock impulse (frame 2)

Thus it is seen that sampling rates many times the vibrational frequency may be required for vibrational analysis.

If the same fractional fringe motion is applied to the case where the object moves from displacement  $a_1$  to displacement  $a_2$  during the time in interval  $\tau$ , it is found the inequality

$$2k (a_2 - a_1) \leq \frac{\pi}{2} \quad (5-7)$$

must be satisfied. Dividing by  $\tau$  reduces (5-7) to the form

$$\tau \leq \frac{\lambda}{8v} \quad (5-8)$$

where  $v$  is the average velocity of the object between time  $t_1$  and  $t_2$ . The velocity can be related to the impulse given the structure. For the experiments conducted at GCO the shutter time of  $20 \times 10^{-6}$  seconds limited velocities to something less than 0.3 cm/sec. before good fringes could be recorded. The sampling period of  $2 \times 10^{-4}$  seconds limited data reduction velocities to less than 0.03 cm/sec. These are extremely low impulse loads and are hardly of interest.

## 6.0 CONCLUSIONS AND RECOMMENDATIONS

In this section an attempt will be made to summarize the results of the previous sections and provide recommendations for additional programs in the general area of vibration analysis. The limitations of the techniques investigated will be summarized and used to explain the observed results and recommended programs.

### 6.1 Steady-State Vibrational Analysis

The use of holography as a replacement for conventional vibrational detectors was clearly demonstrated and verified during the course of the contract. The advantages of holography over conventional detection methods are that a non-contacting measurement is made and the response of the entire body is measured as opposed to individual points as in the case of conventional detectors.

To uniquely determine the vibrational vector on a three-dimensional body requires the use of more than one hologram or one hologram with a wide field-of-view of each point of interest. While in principle this is possible, one advantage of holography over conventional techniques is lost as point-by-point measurements have to be made and correlated. This being the case, it appears the major utility of holography will be as a tool to rapidly determine vibrational frequencies of a structure while at the same time determining the modal characteristics and transfer functions in a qualitative rather than a quantitative manner.

Using conventional techniques the relative phase between points on the vibrating surface cannot be determined. Various phase modulations may be applied to the reference wavefront to obtain information on vibrational phases. The utility of a frequency modulated reference wavefront was demonstrated during the course of this contract. Other forms of phase and amplitude modulation may also be used to determine the relative phases on the vibrating surface.

Work conducted at the University of Michigan has recently shown that if the frequency of the reference beam is translated by the vibrational frequency, the holographically reconstructed image brightness varies as  $J_1^2$  in lieu of the conventional  $J_0^2$ . In this case the nodal regions are dark and the peak-to-peak brightness variation is reduced over the  $J_0^2$  case. This lack of a reference nodal position may make general vibration analysis difficult, but is extremely useful for detecting vibrational motions which are a very small fraction of the operating wavelength. It is estimated that the amplitude detection limit of this technique is in the range of  $\lambda/100$  to  $\lambda/1000$ .

The primary limitations of holographic vibrational analysis are the requirements for a sinusoidal driving function and an extremely low upper limit on vibrational amplitude. To overcome the driving function limitation, it may be possible to

construct a real-time system which is viewed by a TV system with the capability for frequency analysis. The real-time fringe system would be monitored and the video current frequency analyzed before the image is displayed on the TV monitor. The limitations on vibrational amplitude may be overcome with an extension of stroboscopic analysis which is outlined below.

## 6.2 Stroboscopic Analysis

To improve the contrast of the observed real-time fringe system the illumination and reconstruction sources are strobed in synchronism with the vibrational frequency. The fringe system observed has a  $\cos^2$  brightness weighting as opposed to the  $(1 + J_0)$  weighting of conventional real-time holographic vibrational analysis. This weighting was found to be extremely useful when the vibrational amplitudes were larger than 1 or 2 wavelengths as the contrast of the  $1 + J_0$  fringe system was essentially zero. Using strobe techniques the resonant frequencies and amplitudes can be readily determined as opposed to only determining resonant frequencies with conventional real-time viewing. The limitation on peak vibrational amplitude is relaxed with stroboscopic analysis, but is still limited because of the high order fringe system generated which makes data reduction difficult.

The technique of stroboscopic analysis may be extended in two ways to include large vibrational amplitudes. The first is by variation of the time of the illumination strobe relative to the time of peak vibrational amplitude. If the illumination is strobed near the minimum vibrational amplitude position a relatively low order fringe system results. However, knowing the order of the observed fringe system and the timing of the illumination strobe relative to the time of peak amplitude, the peak amplitude can be calculated. A second method is to strobe the illumination at the time of minimal amplitude. However, in this case the strobe pulse is lengthened so as to not stop the observed fringe system. The observed fringe system will then have a  $\sin x/x$  weighting where  $x$  is dependent upon the peak vibrational amplitude and the duty cycle of the illumination strobe.

## 6.3 Shock

During the pursuit of this contract an attempt was made to study the effect of shock loads on simple structures using a high-speed camera and real-time holographic interferometry. The only information obtained was visually interesting when viewed at the slow motion rates of a movie projector, but quantitative data could not be obtained. To obtain quantitative data will require a frame-by-frame analysis of the recorded fringe system. The low data rates used and background noise prevented the reduction of the data obtained in any manner except the qualitative method of movie projection.

It has been shown above that the extreme sensitivity of interferometry limits the utility of the technique of shuttered real-time shock analysis to the case of extremely low level shock, if present-day equipments are used. As equipments

and procedures are developed it will become possible to operate at much higher sampling rates and thus include a larger range of shock phenomenon. However, for the present, it appears that only a very limited class of shock events can be analyzed using shuttered real-time holographic interferometry.

Shock phenomenon may also be analyzed using variations of moire techniques described in the open literature and being investigated at GCO. This particular technique involves the projection of an aerial fringe system onto a surface in such a way that out-of-plane movements of the surface manifest themselves as movements of the fringe system over the surface. The displaced fringe system is compared to the reference fringe system by moire techniques and the out-of-plane movements calculated. The sensitivity of the technique is variable and should prove useful for analysis of shock phenomenon.

#### 6.4 Recommendations

Based upon the above observations, GCO recommends the following items as worthy candidates for further investigation:

1. Investigation of subfringe vibrational amplitude in the ultrasonic range using frequency translation technique,
2. Investigation of large amplitude vibration using strobe techniques, and
3. Investigation of shock and transient events using reduced sensitivities available with moire techniques.

